# SPECTROSCOPY OF THE POTENTIAL ENERGY SURFACES FOR C–H AND C–O BOND ACTIVATION BY TRANSITION METAL AND METAL OXIDE CATIONS

R. B. METZ

*Department of Chemistry, University of Massachusetts Amherst, Amherst, MA 01003, USA*

## CONTENTS



*Advances in Chemical Physics, Volume 138*, edited by Stuart A. Rice

## I. INTRODUCTION

The potential energy surface (PES) determines the course of a chemical reaction, and characterizing PESs for reactions has been a central focus of chemical dynamics [1]. Reaction studies, especially detailed measurements of reaction cross-sections as a function of collision energy or the reactivity of state selected reactants to produce products whose quantum states are measured, provide a great deal of indirect information on the PES for a reaction. However, even relatively simple reactions may involve several intermediates, connected by multiple transition states, and a particular experiment will only be sensitive to some features of the PES. Spectroscopic studies complement bimolecular experiments as they provide a direct probe of a region of the PES. Spectroscopy of reactive PESs presents particular challenges, as the stationary points on the surface correspond to intermediates (local minima) that are often short lived and to transition states (local maxima) that are inherently transient. Our studies of the PES of transition metal ion-molecule reactions are part of a tradition of transition state spectroscopy, which has primarily been used to study reactions of neutrals. Early studies by Brooks, Stwalley, and co-workers looked at far wing absorption by reacting complexes during the course of a harpoon reaction [2–4]. These experiments are extremely challenging, and interpreting the results is complicated by the averaging over impact parameter and orientation inherent in bimolecular reactions. Photoinitiating a reaction from a precursor with a similar geometry to the region of the PES of interest provides a powerful alternative. One advantage is that photoexcitation provides a start time to the reaction, which makes possible time-resolved studies, such as those of Zewail and co-workers [5,6]. A second advantage is that the energy, orientation, and angular momentum (impact parameter) are constrained, and energy-resolved studies can give well-resolved spectra rich in information, although one is limited to studying regions of the PES with good Franck–Condon overlap with the initial complex. In work on neutral metal atom reactions, Polanyi and co-workers [7] and Soep, Visticot, and co-workers [8,9] photoexcite van der Waals clusters, such as Ca(XH), where X is a halide to study the $Ca^* + XH \rightarrow CaX + H$ harpoon reaction. Kleiber and co-workers have studied photodissociation of complexes of alkaline earth cations, $Al^+$ and $Zn^+$ with hydrogen, hydrocarbons, and simple organic molecules, observing several examples where photoexcitation leads to H—H, C—H, or C—C bond activation [10–13]. Photodetachment of a stable negative ion can give information on the corresponding neutral, which may be an intermediate or transition state of a neutral reaction. Brauman and co-workers measured photodetachment cross-sections of hydrogen-bound negative ions to study the transition state of hydrogen-transfer reactions [14]. Photoelectron spectroscopy gives more detailed information. Lineberger and co-workers studied isomerization of vinylidene to acetylene from photoelectron

spectroscopy of $CCH_2^-$ [15], and photoelectron spectroscopy of a strongly bound negative ions, such as $XHY^-$, where X and Y are halogen atoms, allows Neumark and co-workers to study the $X + HY \rightarrow XH + Y$ hydrogen-exchange reaction [16, 17].

Spectroscopy of the PES for reactions of transition metal ($M^+$) and metal oxide cations ($MO^+$) is particularly interesting due to their rich and complex chemistry. Transition metal $M^+$ can activate C—H bonds in hydrocarbons, including methane, and activate C—C bonds in alkanes [18–20]; $MO^+$ are excellent (and often selective) oxidants, capable of converting methane to methanol [21] and benzene to phenol [22–24]. Transition metal cations tend to be more reactive than the neutrals for two general reasons. First, most neutral transition metal atoms have a $d^{x-2}\,s^2$ ground electronic state, and this configuration tends to be nonreactive. This is especially true for the *3d* metals, where the *4s* orbital is significantly larger than the *3d*, so an approaching molecule sees the filled, repulsive *4s* orbital. The reactivity of neutral M with hydrocarbons is correlated to the promotion energy required to form a state with a $d^{x-1}\,s^1$ configuration and the appropriate spin [19]. The ground state of the $M^+$ cations is $d^x\,s^0$ or $d^{x-1}\,s^1$ (and the other configuration often lies at low energy), so this promotion energy is usually low. The second reason for the enhanced reactivity of the ions is the strength of the ion-induced dipole and ion–dipole interaction. This causes the initial $M^+$–reactant interaction to be attractive, leading to a strongly bound entrance channel complex, as shown in Fig. 1. This binding energy is substantial: ~1 eV for late transition metal $M^+$ and $MO^+$ with methane. This also serves to stabilize all of the intermediates (and the barriers separating them) relative to the reactants and products.

Figure 1 highlights several general features of PESs for $M^+$ reactions. After forming the entrance channel complex, the metal typically inserts into a bond in

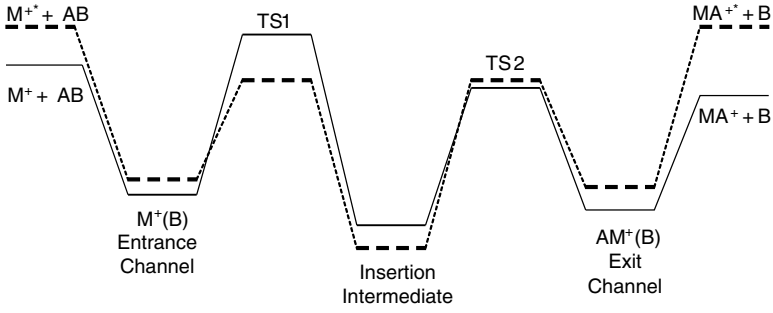


**Figure 1.** Schematic PES for reaction of a transition metal cation $M^+$ with a hydrocarbon AB. The potential for the high spin reaction is shown with solid lines; dashed lines indicate the low spin reaction.

the reactant, leading to one or more insertion intermediates. The situation shown in Fig. 1, in which it is energetically favorable for reaction of a high spin metal to occur through low spin intermediates, is fairly common, especially for the late transition metals. The low spin configurations provide much more flexibility in bonding, as more electrons can be paired. Finally, electrostatic interactions lead to a strongly bound exit channel complex. The PES for these ion molecule reactions differs significantly from those of neutral reactions in that one (and usually several) of these adducts (intermediates, reactant, or product complexes) is significantly more energetically stable than either reactants or products. In our group, we synthesize and cool the intermediates and study them using electronic and vibrational spectroscopy [25].

A wide range of bimolecular experiments have characterized PESs for reactions of transition metal containing ions. Thermal reaction studies identify reaction products and rates, and have been applied to a wide range of reactions to illuminate periodic trends and reveal catalytic cycles [18–20, 24, 26]. In contrast to neutrals, there have been few crossed molecular beam studies of these reactions, although crossed-beam studies have revealed interesting dynamics in competitive C—C versus C—H activation in hydrocarbons and measured the lifetime of the reaction intermediates [27–29]. The charge on ions means that their velocity (and hence collision energy) can be readily varied. The majority of metal ion–ligand bond strengths have been determined by measuring reaction cross-sections as a function of collision energy on guided ion beam instruments [30–32]. Low energy collision induced dissociation of the intermediates gives their energies relative to reactants or products [33–35]. As Fig. 1 shows, an important feature of many reactions of transition metal ions is the participation of PESs with different spin. Reactions of state-selected metal ions measure how spin and electronic configuration affect rates and products [36–38]. Our work on the vibrational and electronic spectroscopy of reactants and reaction intermediates studies complements the collision studies by characterizing the structure and vibrations of these species and, in some cases, measuring bond strengths.

Photoionization of a neutral complex could be a powerful tool for studying the PESs of reactions of transition metal cations, much as photoelectron spectroscopy of negative ions has been applied to transition state spectroscopy of neutral reactions. However, the difficulty of generating tunable vacuum ultraviolet (UV) light with sufficient intensity has hampered these studies. We have measured [39] photoionization efficiencies for FeO and CuO at the Chemical Dynamics beamline of the Advanced Light Source (Lawrence Berkeley National Lab), obtaining ionization energies for the metal oxides and observing low lying quartet states of $FeO^+$. Transitions to these states are optically forbidden from the $FeO^+$ $^6\Sigma$ ground state. These results are detailed in Section III.B. Recent experiments have looked at photoionization of PtC, PtO,

and $PtO_2$. Followup photoelectron spectroscopy studies are planned, to measure vibrational frequencies and low lying electronic states of the cations.

The PES for even a simple transition metal ion reaction is quite complex; experiments alone cannot characterize it and electronic structure theory is required. Calculations of reactive PESs are inherently challenging, as they involve partially made and –broken bonds. Calculations involving transition metals are even more difficult, due to the presence of several unpaired electrons and large number of low lying electronic states. Transition metal reactions frequently involve multiple spin states. Figure 1 shows a fairly common case, in which ground state, high spin $M^+$ reacts to form ground-state, high spin $MA^+$, yet the reaction proceeds through low spin intermediates. Modeling such a reaction requires accurately calculating the high and low spin surfaces and their relative energies, as well as the coupling between the surfaces. Spectroscopy of the reactants and reaction intermediates provides a rigorous test of the accuracy of computational methods.

## II. EXPERIMENTAL METHODS

We use laser photofragment spectroscopy to study the vibrational and electronic spectroscopy of ions. Our photofragment spectrometer is shown schematically in Fig. 2. Ions are formed by laser ablation of a metal rod, followed by ion molecule reactions, cool in a supersonic expansion and are accelerated into a dual TOF mass spectrometer. When they reach the reflectron, the mass-selected ions of interest are irradiated using one or more lasers operating in the infrared (IR), visible, or UV. Ions that absorb light can photodissociate, producing fragment ions that are mass analyzed and detected. Each of these steps will be discussed in more detail below, with particular emphasis on the ions of interest.

### A. Ion Production

Ions are produced in a Smalley-type laser ablation source [40,41]. The frequency-doubled output (532 nm) of a pulsed Nd:YAG laser is loosely focused

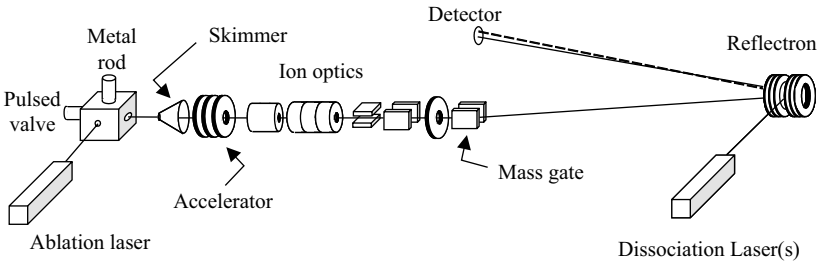


**Figure 2.** Time-of-flight (TOF) photofragment spectrometer.

onto a rotating and translating metal rod. Ablation produces transition metal ions $M^+$, which then react with an appropriate precursor entrained in a pulse of gas introduced through a piezoelectric pulsed valve [42]. Simple metal–ligand complexes $M^+L$ where the ligand is a stable molecule [e.g., $V^+$ $(CO_2)$] are produced using 0.05–5% ligand seeded in an inert carrier, such as helium or argon at a backing pressure of 1–5 atm.

Most of the ions we study have covalent bonds to the metal (e.g., $MO^+$, $[HO{-}M{-}CH_3]^+$). These ions are synthesized via ion molecule reactions, and our choice of synthetic precursors is guided by the extensive literature on ion molecule reactions, typically carried out under single-collision conditions in ion cyclotron resonance (ICR) spectrometers [18, 43]. Although conditions in our ablation source are very different from those in an ICR, we generally observe the same products (other than, of course, the ablation source also produces cluster ions). Thus, for example, $FeO^+$ is produced by reaction of $Fe^+$ with nitrous oxide [44]. Studying the intermediates of a reaction presents a special challenge, as they are all isomers and thus cannot be separated in a mass spectrometer. In our study of the intermediates of the $FeO^+ + CH_4$ reaction [45] (Section III.C) it was critical to find precursors that selectively form each intermediate. Our choices were based on the extensive study of Schröder et al., who produced several of the intermediates by reacting $Fe^+$ with a variety of neutral molecules in an ICR [46]. They identified the resulting ions based on fragments produced after collision-induced dissociation (CID). Again, we are generally able to produce the desired intermediate using the same reaction. For example, the $[H_2C{=}Fe{-}OH_2]^+$ intermediate is synthesized by the reaction of $Fe^+$ with acetic acid or, with less efficiency and specificity, *n*-propanol. Reaction of $Fe^+$ with methanol efficiently produces $[HO{-}Fe{-}CH_3]^+$; acetic acid and *n*-propanol also give modest yields of this isomer. In each case, we characterize the ion formed through its dissociation pathways and electronic and vibrational photodissociation spectrum [45].

Once formed, ions travel through a short tube and supersonically expand into the source vacuum chamber. This cools the ions, reducing spectral congestion due to transitions from excited rotational and vibrational states. The molecular beam is then skimmed and ions pass into the differential pumping chamber. We have measured rotational temperatures of 8 K for $FeO^+$ [47] and 12 K for $V^+(OCO)$ [48] although the supersonic expansion is not at equilibrium, so the rotational-state distribution has a small component at a higher temperature, which is not unusual for an ablation source [49]. At these low temperatures, weakly bound cluster ions are readily produced. Vibrational spectroscopy of $V^+(OCO)_n$ and $Fe^+(CH_4)_n$ is discussed in Sections IV and V. When using argon (Ar) as the carrier gas, cluster ions containing argon can be formed. As a result, we study vibrations of the of $[HO{-}Fe{-}CH_3]^+$ insertion intermediate by measuring the vibrational spectrum of $[HO{-}Fe{-}CH_3]^+(Ar)_n$ $(n{=}1{,}2)$

(Section III.C). Using a rotational temperature to characterize an ion source can be misleading, as the reactions used to form the ions of interest can be quite exothermic, producing vibrationally and even electronically excited ions. These degrees of freedom are more difficult to cool than rotations. Transitions from vibrationally excited molecules provide very useful information, if they can be identified and analyzed. Hot $FeO^+$ (produced using 3% $N_2O$ in helium) has a $\nu' = 1 \leftarrow \nu'' = 1$ sequence band that disappears when 15% $N_2$ is added to the carrier gas [47]. This sequence band allows us to measure the ground-state vibrational frequency $\nu_0'' = 838 \pm 4\,\mathrm{cm}^{-1}$. Similarly, by adjusting the delay between the ablation laser and the pulsed valve, we can observe [48] the $\nu_3' = 0 \leftarrow \nu_3'' = 1$ hot band in $V^+(OCO)$, which gives the frequency of the metal–ligand stretch in the ground electronic state $\nu_3'' = 210\,\mathrm{cm}^{-1}$.

After the skimmer, ions are extracted along the beam axis using a pulsed electric field, then accelerated to 1800-V kinetic energy. This is a coaxial version of the classic orthogonal Wiley–McLaren TOF mass spectrometer [50]. It is convenient to have the source and flight tube grounded, so, after acceleration, the ions are rereferenced to ground potential [51]. This is accomplished by having the rereferencing tube at -1800 V potential as the ion cloud enters, then pulsing it to ground prior to the ions' exit using a potential switch [52]. An Einzel lens and deflectors guide the ions through an aperture into the detector chamber. A final deflector allows the ion beam to traverse the 5° angle through the reflectron and to the detector. When the deflector is off, $<0.1\%$ of the incident ions reach the detector. Applying a pulsed voltage to the deflector allows only ions within a few mass units of the ion of interest to reach the detector, forming an effective mass gate. This is essential as, without the mass gate, peaks from lighter ions, particularly the large $M^+$ peak, distort the baseline for the rest of the mass spectrum.

Ions are photodissociated at the turning point [53] of the reflectron [54, 55] with pulsed lasers. Photofragment ions and undissociated parent ions (dashed line in Fig. 2) reaccelerate out of the reflectron and strike a 40-mm diameter dual microchannel plate detector. Masses of parent and fragment ions are determined from their flight times. Two laser systems were employed for the studies described here. Electronic spectra were obtained using the unfocused output of a pulsed, tunable Continuum dye laser pumped by a Continuum Nd:YAG laser. With mixing and doubling crystals, this laser system is tunable from 220 to $>900$ nm with $< 0.08\text{-cm}^{-1}$ line width. A LaserVision IR OPO/OPA pumped by an injection seeded Nd:YAG laser produces light in the near- and mid-IR for vibrational spectra. The IR laser system uses a 532-nm pumped OPO, followed by a 1064-nm pumped OPA. In the mid-IR, it is tunable from $\sim$2100 to $>4000\,\mathrm{cm}^{-1}$, with 0.3-$\mathrm{cm}^{-1}$ line width. It produces $\sim$3 mJ/pulse near $2400\,\mathrm{cm}^{-1}$ and $\sim$10 mJ/pulse near $3800\,\mathrm{cm}^{-1}$. The lasers operate at 20-Hz repetition rate.

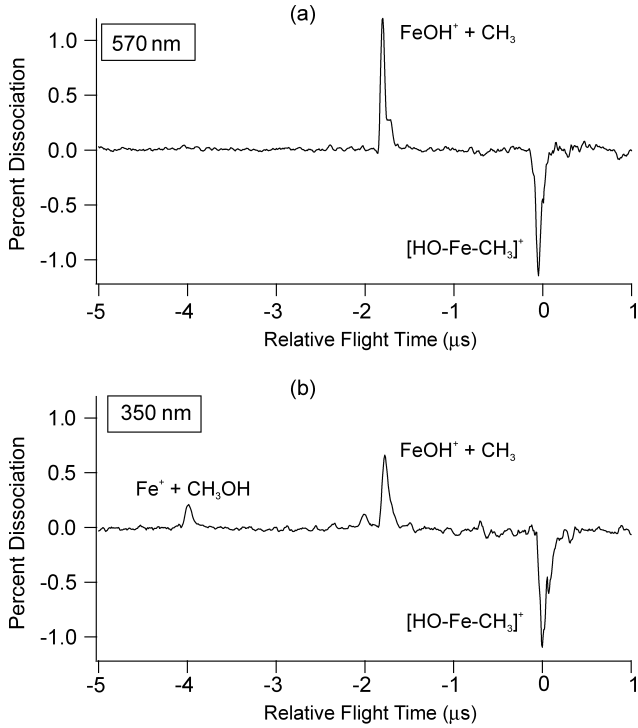


**Figure 3.** Difference mass spectrum of the $[HO{-}Fe{-}CH_3]^+$ insertion intermediate at photolysis wavelengths of 570 nm (a) and 350 nm (b). Simple Fe–C bond fission is observed at both wavelengths, but photolysis at 350 nm also triggers the half reaction to produce $Fe^+ +$ methanol ($CH_3OH$).

The ion signal is amplified, collected on a digital oscilloscope or a gated integrator, and averaged using a LabView-based program. Subtracting mass spectra collected with the dissociation laser blocked from those when it is unblocked produces a *difference mass spectrum*. As shown in Fig. 3, this allows immediate identification of the dissociation channels active at a particular wavelength, along with their relative importance. Mass resolution is $m/\Delta m \sim 200$ for fragment ions, although the large parent ion signal can make it difficult to detect H atom loss from heavy ions, such as $AuCH_2^+$.

The shape of the fragment peak in the difference mass spectrum can be affected by kinetic energy release and the dissociation rate. Significant kinetic energy release leads to broadening, while slow dissociation leads to tailing. We have not yet observed broadening in photofragments of singly charged ions, probably because the long-range attraction between the fragments and the large number of available product quantum states both favor low kinetic

energy release. We do, however, observe significant broadening in singly charged fragments formed by photodissociation of dications, where the Coulomb repulsion between the fragments leads to kinetic energy releases of 80–170 kJ $mol^{-1}$ [56–58]. If an ion is photoexcited, then travels some distance through the reflectron before it dissociates, its flight time will lie between those of the parent ion and prompt-dissociating fragments. The fragment peak in the difference mass spectrum will then exhibit an exponential tail whose time constant depends on the dissociation rate. In our apparatus, tailing should be observed for dissociation lifetimes in the range $\sim$50 ns to $\sim$3 μs. We have not observed tailing for any singly charged, metal-containing ions, indicating photodissociation lifetimes $< 50$ ns. Larger ions do show tailing, for example, the ethylbenzene radical cation near 450 nm [59] and $Co^{2+}(CH_3OH)_4$ at 570 nm [58] from work in our group, and $Fe_3$coronene$^+$ at 532 nm [60] from work by Duncan's group.

Monitoring the yield of a particular fragment ion as a function of laser wavelength and normalizing to parent ion signal and laser fluence yields the *photodissociation spectrum*. This is the absorption spectrum of those ions that photodissociate to produce the fragment being monitored. The photodissociation spectrum is obtained by monitoring the fragment ion signal with a gated integrator or, if the fragment ion signal is very small, measuring the area under the fragment peak in the difference mass spectrum using numerical integration and then normalizing to the parent signal and laser fluence.

### B. Electronic Spectroscopy

The ions we study typically have several unpaired electrons and consequently have many excited electronic states. This high density of states, along with peak broadening due to photoinduced reactions, fast internal conversion and rapid dissociation can lead to broad, featureless electronic photodissociation spectra. These cases provide a strong impetus for vibrational spectroscopy (described below). However, broad spectra do contain useful thermodynamic information, as one-photon dissociation of internally cold ions requires the photon energy to exceed the strength of the bond being broken. The photodissociation onset thus provides an upper limit to the true, thermodynamic bond strength [30–32, 61]. The high density of electronic states in ions with a coordinatively unsaturated transition metal center means that they are likely to absorb widely in the visible and near UV. As a result of this broad absorption and strong coupling between states near the dissociation limit, these ions often photodissociate at the thermodynamic threshold, and the photodissociation onsets give bond strengths precise to 5 kJ/mol or better [25, 62–64]. Photodissociation studies can thus complement bond strengths measured with collisional methods [32] such as endothermic reactions or collision induced dissociation in guided ion beams. In general, collisional methods are preferred for measuring bond strengths, as they

have higher throughput and are more generally applicable because they do not rely on specific absorption properties of the molecule. The exception is those ions for which the photodissociation spectrum exhibits vibrational structure that completely converges to a diabatic dissociation limit. This has been seen for $VAr^+$ and $CoAr^+$; the dissociation limit can be determined with spectroscopic accuracy, giving bond strengths with $<0.1$-kJ $mol^{-1}$ precision [65–67]. The methods used to measure ion thermochemistry are compared in an excellent review by Ervin [30].

Fortunately, many of the ions we study predissociate, giving photodissociation spectra with resolved vibrational progressions and, in some cases, residual rotational structure. Electronic spectroscopy of the $FeO^+$ reactant and the $[HO{-}Fe{-}CH_3]^+$ intermediate of the $FeO^+ + CH_4 \rightarrow Fe^+ + CH_3OH$ reaction is discussed in Section III, while the electronic spectroscopy and coupling between high and low spin states of $V^+(OCO)$ is covered in Section IV. Analysis of the electronic photodissociation spectrum gives detailed information on the excited-state potential energy surface(s), coupling between electronic states, and the geometry of the ion.

If an ion predissociates, then the rotational congestion and vibrational sequence bands can determine the resolution of the photodissociation spectrum. Most of the ions we study are quite rotationally cold, irrespective of the source conditions. However, varying the source conditions can greatly affect the vibrational temperature of the ions. As noted above, vibrational hot bands can be very useful, characterizing low frequency vibrations in the ground electronic state. More commonly, the peaks in the spectrum are simply broadened due to overlapping vibrational sequence bands. Helium, the typical buffer gas, is rather poor at cooling vibrations, so we often add $<10\%$ of a polyatomic molecule to enhance vibrational and electronic cooling. Adding $O_2$ eliminates an electronic hot band in $PtO^+$ and gives a much sharper dissociation onset in $CoCH_2^+$, again due to cooling metastable excited electronic states [63,68]. We have used $CF_4$, which is rather inert, for vibrational cooling in $Au^+(C_2H_4)$ [69]. The unimolecular dissociation rate of ethylbenzene cation is strongly dependent on the available energy. To produce vibrationally cold ions, we form them first by charge transfer from $Pt^+$, which is nearly thermoneutral, and also include $CO_2$ in the carrier gas [59]. In producing cluster ions, more concentrated mixes are not always better. We produce cold $V^+(OCO)_5$ using 5% $CO_2$ in helium. This same mix produces $V^+(OCO)$, which is fairly hot, as, in order to get good yields of the smaller clusters, we have to adjust the delay between the ablation laser and pulsed valve to have lower gas pressure in the ablation region. Using only 0.1% $CO_2$ in helium produces plenty of $V^+(OCO)$, and it is cold [48].

Photofragment spectroscopy is extremely sensitive, but it has the disadvantage that one is only sensitive to absorption that leads to photodissociation. For single-photon experiments, this means that one is restricted

to studying electronic states that lie above the dissociation limit, and the lifetime of these states usually determines the resolution of the spectrum. We, along with several other groups, have developed techniques to measure the spectroscopy of states that lie below the dissociation limit, with laser-limited resolution. We have used resonance-enhanced photodissociation (REPD) spectroscopy to study the electronic spectrum of $FeO^+$ near 14,000 $cm^{-1}$. One photon promotes the molecule to an excited electronic state; absorption of a second photon leads to dissociation. We obtain the rotationally resolved spectrum, with 0.05-$cm^{-1}$ resolution, which allows us to measure the rotational constants (and bond lengths) in the ground and excited electronic states. The results are discussed in more detail in Section III.B. Brucat and co-workers used REPD to study charge-transfer transitions in $CoO^+$ [49]. One disadvantage of REPD is the low dissociation yield. For $FeO^+$, we obtain 0.1% dissociation at a peak, which restricts us to studying ions that can be produced in abundance. A second consideration is power broadening. For the $FeO^+$ study, the UV laser was not focused and was attenuated to avoid saturating the more intense transitions. Using two different wavelengths helps to avoid this problem, as the fluence of the laser exciting the bound–bound transition can be low, while that of the second laser is much higher. In addition, one can access a much broader range of electronic states, as one is not restricted to those that lie above 50% of the dissociation energy. An excellent example of two-color resonance enhanced photodissociation is the study of vibronic transitions in $Ni_2^+$ by Brucat and co-workers [70].

Another method to measure electronic spectra of ions below the dissociation limit is to photoexcite molecules relatively weakly bound to a ligand. For example, photofragmentation of $FeCH_2^+(H_2O)$ in the visible probes electronic states of the $FeCH_2^+$ chromophore that lie below $D_0(Fe^+–CH_2) = 28500\ cm^{-1}$ [31, 63]. Absorption of 14,000–20,000-$cm^{-1}$ photons leads to loss of $H_2O$. The resulting spectrum is vibrationally resolved, but the peaks are $\sim$300 $cm^{-1}$ wide. The REPD of $FeCH_2^+$ shows a similar vibrational progression, shifted 1740 $cm^{-1}$ to the red. [45]. This shift is due to the different binding energies of $H_2O$ to the ground and excited states of $FeCH_2^+$. The peaks in the REPD spectrum are also 300 $cm^{-1}$ wide, probably due to rapid internal conversion of the excited state. In their photofragment study of the $ZrO^+(CO_2)$ and $ZrO^+(N_2)$ complexes, obtained by monitoring loss of $CO_2$ or $N_2$, Brucat and co-workers observe beautifully resolved photodissociation spectra from 14,900 to 17,700 $cm^{-1}$, with progressions in the Zr—O stretch, as well as the ZrO—ligand stretch and rock [71]. This technique provides a way to study the electronic spectroscopy of $ZrO^+$ far below its dissociation limit. Similarly, we observe a well-resolved spectrum in $TiO^+(CO_2)$ from 14,000 to 17,300 $cm^{-1}$, which probes a $^2\Pi \leftarrow {}^2\Delta$ transition in $TiO^+$ [72].

### C. Vibrational Spectroscopy

Electronic spectroscopy of jet-cooled molecules is an excellent tool to characterize excited electronic states of molecules, but it rarely gives information on vibrations in the *ground* electronic state. Vibrational (IR) spectroscopy is the tool of choice to study bonding in the ground electronic state. In electrostatically bound entrance channel complexes, such as $M^+(CH_4)$, vibrational spectroscopy illuminates the mechanism of C—H bond activation by measuring how interaction with the metal center affects bonds in the reactant. Similarly, vibrational spectroscopy of reaction intermediates elucidates the mechanism of ligand activation by the metal center. An additional advantage is that vibrational spectroscopy gives well-resolved spectra even in quite complex molecules, such as $M^+$ bound to several ligands, where the electronic spectrum is usually featureless [73]. As a result, vibrational spectroscopy of ions has chiefly been applied to studying *noncovalent interactions* in solvated cluster ions [73–92]. Vibrational spectroscopy has been used to reveal the structure of products and intermediates of ion molecule reactions [93, 94] as well as of intracluster reactions [76, 95]. We have used vibrational spectroscopy to study covalently bound reaction intermediates, such as $[HO—Fe—CH_3]^+$ (Section III.C), and noncovalent complexes, such as $V^+(OCO)$ and $Fe^+(CH_4)_n$ (Sections IV and V). These studies were carried out using an IR OPO/OPA laser system that is pumped by an injection-seeded Nd:YAG laser. The IR laser system uses a 532-nm pumped OPO and a 1064-nm pumped OPA to produce tunable light from 2100 to $>4000\,cm^{-1}$, with 0.2-$cm^{-1}$ line width and $\sim$3 mJ/pulse near 2400 $cm^{-1}$ and 8 mJ/pulse near 3500 $cm^{-1}$. Free electron lasers, such as FELIX (Netherlands) and CLIO (France), produce very high fluences down to $\sim$600 $cm^{-1}$. This wide spectral range has allowed the characterization of many ions that have several potential isomers [74, 81, 93, 94, 96]. Free electron lasers have disadvantages: beam time is limited and the spectra tend to be broad due to the 2% bandwidth of the light and high fluences required for efficient IR multiphoton dissociation.

Photofragment spectroscopy requires that the ion dissociate, which is a challenge as most of the ions we wish to study have significant binding energies: for example, $V^+(OCO)$ is bound by 6000 $cm^{-1}$ [33]. Groups in this field have developed a toolbox of complementary techniques to measure IR spectra of strongly bound ions [74]. No one method is perfect or completely general, but at least one method should work on any given ion. Because absorption of several IR photons can dissociate even strongly bound ions, *resonance enhanced IR multiphoton dissociation (IRMPD)* has proven a useful tool for studying the spectroscopy of ions since early work on organic ions using $CO_2$ lasers [97]. Transition metal containing systems have also been studied using $CO_2$ lasers [98–101]. The high fluences available from IR OPOs and free-electron lasers make IRMPD an attractive technique. Efficient IRMPD requires fairly rapid

intramolecular vibrational redistribution (IVR), to ensure that vibrationally excited molecules continue to absorb at the resonant wavelength and also to efficiently transfer energy from the vibration excited to the dissociation coordinate. Small molecules and clusters tend to have high binding energies and low vibrational density of states (and hence small IVR rates); larger molecules are better candidates for IRMPD due to their higher densities of states and more rapid IVR. For example, Duncan and co-workers observe no signal in IRMPD of $Fe^+(CO_2)$, weak signal from $Fe^+(CO_2)_2$, and strong signals in larger clusters, attributing this to slow IVR in the small clusters [102]. Similarly, $[HO{-}Fe{-}CH_3]^+$ is not a good candidate for IRMPD studies. We observe very small amounts of multiphoton dissociation: only 0.1% dissociation in the O—H stretching region. Also, power broadening and preferential photodissociation of hotter ions in the beam lead to a broad, poorly resolved spectrum.

"*Argon tagging*" is a version of the "spectator spectroscopy" developed by Lee and co-workers [103] in which the ion of interest is clustered with one or more argon atoms. The IR absorption by the ion core leads to vibrational predissociation and loss of the tag. The choice of argon as the tag is a compromise: Argon has sufficiently weak binding to ensure one-photon dissociation and to minimize perturbations of the vibrational spectrum, yet binds sufficiently strongly to allow production of usable quantities of tagged ions. Argon tagging has been extensively developed by Johnson and co-workers for the spectroscopy of negative ions [78, 104–107] and has been used by Lisy and co-workers to study $Cs^+(H_2O)$ and $Li^+(H_2O)$ [86,88] and Duncan and co-workers to study many ions, including $M^+(CO_2)_n$ (M = Al, Fe, Mg, Ni, V) [76, 77, 102, 108–112]. We have used this technique to measure the O—H and C—H stretching vibrations of $[HO{-}Fe{-}CH_3]^+$ (Section III.C). Neon-tagged ions are more challenging to produce, but the weaker binding is an advantage in studying low frequency vibrations and also gives smaller perturbations [79]. Helium tagging leads to the smallest perturbations and has been used to measure vibrational spectra of vanadium oxide cations using a free-electron laser [113].

Vibrationally mediated photodissociation (VMP) can be used to measure the vibrational spectra of small ions, such as $V^+(OCO)$. Vibrationally mediated photodissociation is a double resonance technique in which a molecule first absorbs an IR photon. Vibrationally excited molecules are then selectively photodissociated following absorption of a second photon in the UV or visible [114–120]. With neutral molecules, VMP experiments are usually used to measure the spectroscopy of regions of the excited-state potential energy surface that are not Franck–Condon accessible from the ground state and to see how different vibrations affect the photodissociation dynamics. In order for VMP to work, there must be some wavelength at which vibrationally excited molecules have an electronic transition and photodissociate, while vibrationally unexcited molecules do not. In practice, this means that the ion has to have a

vibrationally resolved photodissociation spectrum due to predissociation [as is the case for $V^+(OCO)$] or that the photodissociation spectrum have a sharp onset (e.g., at the bond strength, as for $FeCH_2^+$, $AuCH_2^+$ and several other ions we have studied) [25, 63, 121]. This is not always the case, or the electronic transition may be weak, or lie at an inconvenient wavelength, so VMP is less generally applicable to ion spectroscopy than IRMPD or tagging. However, VMP has the great advantage that it can be used to measure vibrational spectra of unperturbed ions with resolution limited only by the laser line width. Section IV discusses our use of VMP to measure the OCO antisymmetric stretch in $V^+(OCO)$ and to see how exciting vibronic transitions involving this vibration affect the photodissociation dynamics.

## III. METHANE–METHANOL CONVERSION BY $FeO^+$

Methane cannot be liquefied by pressure alone, it must also be cooled, which makes it awkward to transport. Therefore there has been a great deal of effort directed toward direct conversion of methane to an easily transportable and more synthetically useful liquid, such as a larger hydrocarbon or methanol [122–144]. Direct conversion of methane to methanol is also of great fundamental interest as the simplest alkane oxidation. Although no direct, efficient methane–methanol conversion scheme has yet been developed [122], significant advances have been made using iron-based catalysts. Wang and Otsuka have achieved high catalytic selectivity for direct oxidation of methane to methanol using an $FePO_4$ catalyst with $N_2O$ and $H_2/O_2$ as the oxidizing agents, but the reaction yield is low [125, 126]. Other approaches that have achieved modest success include direct oxidation by $N_2O$ in a plasma [127], oxidation of methane to a methyl ester using a platinum catalyst [128, 129], and direct methane–methanol conversion using an iron-doped zeolite [130]. Methanogenic bacteria efficiently convert methane to methanol. The reaction is catalyzed by the enzyme methane monooxygenase (MMO), which contains non-heme iron centers at the active site [131–133].

In 1990, Schröder and Schwarz reported that gas-phase $FeO^+$ directly converts methane to methanol under thermal conditions [21]. The reaction is efficient, occuring at $\sim$20% of the collision rate, and is quite selective, producing methanol 40% of the time ($FeOH^+ + CH_3$ is the other major product). More recent experiments have shown that $NiO^+$ and $PtO^+$ also convert methane to methanol with good efficiency and selectivity [134]. Reactions of gas-phase transition metal oxides with methane thus provide a simple model system for the direct conversion of methane to methanol. These systems capture the essential chemistry, but do not have complicating contributions from solvent molecules, ligands, or multiple metal sites that are present in condensed-phase systems.

Bond activation by transition metals is a complex process, as it often involves making and breaking several bonds and can occur on multiple, coupled potential

energy surfaces. Detailed understanding of the mechanism requires many experiments, as each is sensitive to only part of the potential energy surface, but experiments alone are not sufficient: Accurate calculations are also required. Studies of small model systems that retain the essential chemistry are necessary, as they are the systems for which we can carry out the most detailed experiments and highest level calculations, allowing us to assess the reliability of competing theoretical methods. These methods can then be used to predict mechanisms for more complex, condensed-phase reactions for which we have limited experimental data and to help develop improved catalysts.

Methane-to-methanol conversion by gas-phase transition metal oxide cations has been extensively studied by experiment and theory: see reviews by Schröder, Schwarz, and co-workers [18, 23, 134, 135] and by Metz [25, 136]. We have used photofragment spectroscopy to study the electronic spectroscopy of $FeO^+$ [47, 137], $NiO^+$ [25], and $PtO^+$ [68], as well as the electronic and vibrational spectroscopy of intermediates of the $FeO^+ + CH_4$ reaction.[45, 136] We have also used photoionization of FeO to characterize low lying, low spin electronic states of $FeO^+$ [39]. Our results on the iron-containing molecules are presented in this section.

### A. Reaction and Computational Studies: Mechanism

Figure 4 shows a schematic potential energy surface for the conversion of methane to methanol by $FeO^+$. The sextet (high spin) reaction path is indicated by a solid line and the quartet (low spin) path is dotted. The minor pathway leading to $FeCH_2^+ + H_2O$ is not shown. The relative energies of reactants and products are based on experiment [138]. The energies of intermediates are based on our calculations [45, 139] at the B3LYP/6-311+G(d,p) level, and the energies of transition states are relative to the previous intermediate, as calculated by Yoshizawa et al. [140]. Recent calculations in our group at the CCSD(T)/6-311+G(3df,p) and B3LYP/6-311+G(3df,p) level give similar results, but predict that the quartet and sextet states of the insertion intermediate have very similar energies [141]. Our calculations are an extension of computational studies at the B3LYP/6-311G(d,p) level by Yoshizawa et al. on methane activation by $FeO^+$ [142–144] and the other first-row $MO^+$ [140, 145]. Schröder et al. [46] and Fiedler et al. [146] have also carried out calculations on methane–methanol conversion by $FeO^+$ and the late first-row transition metals, respectively.

The mechanism that has been developed for the conversion of methane to methanol by $FeO^+$ is an excellent example of the synergy between experiment and theory. This mechanism includes two key concepts: concerted reaction involving the critical $[HO{-}Fe{-}CH_3]^+$ insertion intermediate and two-state reactivity. The reaction proceeds as follows: electrostatic interaction between $FeO^+$ and methane produces the $[OFe\cdots CH_4]^+$ entrance channel complex.

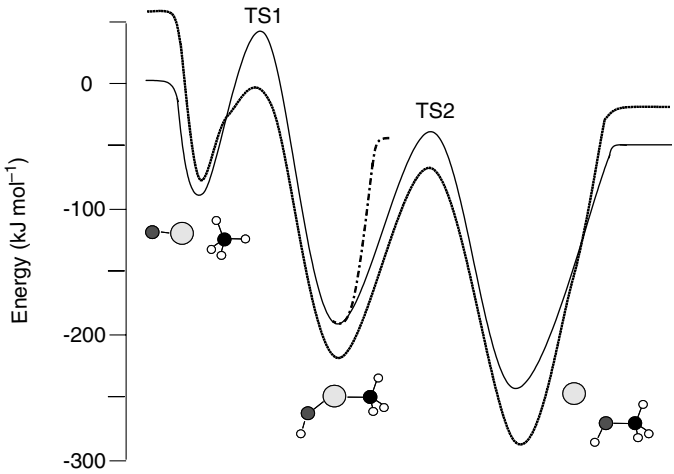


**Figure 4.** Schematic potential energy surface for the reaction of $FeO^+$ with methane. The solid line indicates the sextet surface; the quartet surface is shown with a dotted line, in each case leading to the production of $Fe^+ + CH_3OH$. The dashed line leads to formation of $FeOH^+ + CH_3$. The pathway leading to the minor $FeCH_2^+ + H_2O$ channel is not shown. Schematic structures are shown for the three minima: the $[OFe\cdots CH_4]^+$ entrance channel complex, $[HO{-}Fe{-}CH_3]^+$ insertion intermediate, and $Fe^+(CH_3OH)$ exit channel complex. See text for details on the calculations on which the potential energy surface is based.

Depending on the level of theory, the iron coordinates to methane in an $\eta_2$ or $\eta_3$ configuration, and weakens the proximate C—H bonds by accepting electron density from C—H $\sigma$ bonding orbitals and backdonating electron density to C—H antibonding orbitals. At transition state TS1 the strong C—H bond in methane is being replaced by two bonds: a strong O—H bond and a fairly weak Fe—C bond. Although both the reactants and products are high spin, at thermal energies the reaction occurs through low spin intermediates [143,144], as the high spin TS1 lies significantly above the reactants. This ''two-state reactivity'' has been extensively studied by Shaik and co-workers, especially in the exothermic, but very inefficient, $FeO^+ + H_2 \rightarrow Fe^+ + H_2O$ reaction [147–150]. The *efficiency* of the reaction is determined by the likelihood that reactants will cross TS1. This is determined by the energy of the quartet TS1, as well as by the probability that the initially formed sextet entrance channel complex will undergo a spin change to the quartet state. Shiota and Yoshizawa have calculated [144] the spin–orbit coupling in the entrance channel complex to be a modest $\sim$130 cm$^{-1}$. This and the lifetime of the $[OFe\cdots CH_4]^+$ entrance channel complex determine the likelihood of crossing to the quartet surface. The low efficiency of the $FeO^+ + H_2$ reaction is due to the short lifetime of the entrance channel complex. The TS1 leads to the key insertion intermediate

$[HO{-}Fe{-}CH_3]^+$, which can dissociate to produce $FeOH^+ + CH_3$ or can undergo migration of a methyl group via TS2 to produce the iron–methanol exit channel complex $[Fe(CH_3OH)]^+$, which subsequently dissociates. The *selectivity* of the reaction between methanol and methyl radical products is primarily determined by the energy of TS2 relative to methyl radical products. Because methyl radical is produced by simple bond fission of the insertion intermediate, it is entropically favored over the methanol channel, which occurs through the tighter transition state TS2. Thus, if TS2 is at an energy close to or above methyl products, the reaction will overwhelmingly produce $MOH^+ + CH_3$, as is observed for $MnO^+$ [134, 145]. For $FeO^+$, TS2 lies somewhat below methyl radical products, so the two pathways are competitive at thermal energies, but increased translational energy strongly favors the methyl radical pathway [151]. Producing quartet $Fe^+ + CH_3OH$ from sextet reactants is endothermic, so a second spin change is required to produce exothermic sextet products. Previously, most discussions assumed that this occurs in the $Fe^+(CH_3OH)$ exit channel complex. However, Shiota and Yoshizawa calculate [144] that the spin–orbit coupling in this complex is only $0.3\,cm^{-1}$. They suggest that the second spin change occurs in the insertion intermediate, which has a spin–orbit coupling of $\sim 20\,cm^{-1}$. Our vibrational spectroscopy experiments on the insertion intermediate support this idea, as our results suggest that the quartet and sextet states of $[HO{-}Fe{-}CH_3]^+$ are both formed in the molecular beam and can likely interconvert. In order to characterize $FeO^+$ we have measured the electronic spectroscopy of predissociative and bound states, as well as photoionization of neutral FeO. We have also studied the electronic and vibrational spectroscopy of the $[HO{-}Fe{-}CH_3]^+$ intermediate.

## B. Spectroscopy of $FeO^+$

### 1. *Electronic Spectroscopy of Predissociative States*

In 1986 Freiser and co-workers measured the photodissociation spectrum of $FeO^+$ in an ion cyclotron resonance spectrometer using a lamp–monochromator as their light source. They observed a gradual onset at $\sim 420$ nm leading to a sharp peak near 350 nm ($28{,}600\,cm^{-1}$) whose width was determined by the 10-nm resolution of their instrument [61]. More recent guided ion beam measurements place $D_0(Fe^+{-}O)$ at $28{,}000 \pm 400\,cm^{-1}$ [31]. We produce $FeO^+$ by reacting $Fe^+$ with $N_2O$ and measure its photodissociation spectrum from $\sim 28{,}000$ to $> 30{,}000\,cm^{-1}$. Figure 5 shows the origin of the $^6\Sigma \leftarrow X\ ^6\Sigma$ band, which lies just above the dissociation limit. The partially resolved rotational structure in the peak can be simulated to obtain rotational constants for the upper state, using the known (see below) constants for the ground state [47,137]. The simulation (dashed lines) gives a bond length $r_0' = 1.664$ Å and the spin–spin splitting constant $\lambda' = 0.60\,cm^{-1}$ for the upper state. The resolution is limited to

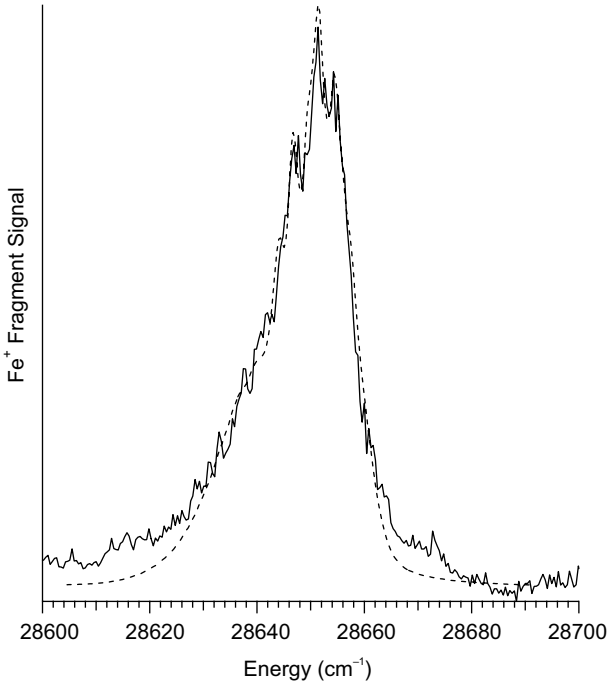


**Figure 5.** Photodissociation spectrum of $^{56}FeO^+$. The 0–0 vibrational transition of the $^6\Sigma \leftarrow X^6\Sigma$ band (solid line) and best-fit simulation (dashed line) are shown.

1.5 $cm^{-1}$ by the 3.5-ps predissociation lifetime of the excited state. The $v' = 1$ peak is observed 662 $cm^{-1}$ higher in energy and is 40 $cm^{-1}$ wide, dissociating in 140 fs. By producing the ions using helium as the carrier gas at low backing pressure, we minimize vibrational cooling and observe the $v' = 1 \leftarrow v'' = 1$ transition at 28,473 $cm^{-1}$, which allows us to measure the vibrational frequency in the ground electronic state $\nu_0'' = 838\ cm^{-1}$ [47].

### 2. *Resonance-Enhanced Photodissociation: $FeO^+$ States Below the Dissociation Limit*

Unfortunately, predissociation of the excited-state limits the resolution of our photodissociation spectrum of $FeO^+$. One way to overcome this limitation is by resonance enhanced photodissociation. Molecules are electronically excited to a state that lies below the dissociation limit, and photodissociate after absorption of a second photon. Brucat and co-workers have used this technique to obtain a rotationally resolved spectrum of $CoO^+$ from which they derived rotational

constants for the $^5\Delta_4$ ground state and the $^5\Pi_3$ and $^5\Phi_5$ excited states [49]. We carried out time-dependent density functional theory calculations (TD–DFT) using the B3LYP hybrid density functional to see if $FeO^+$ has excited electronic states in the relevant energy range. The TD–DFT results, shown in Fig. 6, predict an excited $^6\Sigma$ state near 27500 $cm^{-1}$, with a bond length similar to the ground state. These predictions are in excellent agreement with our observed $^6\Sigma$–$^6\Sigma$ transition. At lower energy, the calculations predict three $^6\Pi$ states with equilibrium bond lengths significantly longer than the ground state. A vertical transition to the lowest $^6\Pi$ state should occur at about one-half of the dissociation energy, making this state a good candidate for resonance enhanced $(1 + 1)$ photodissociation (REPD) studies. Figure 7 shows a portion of the REPD

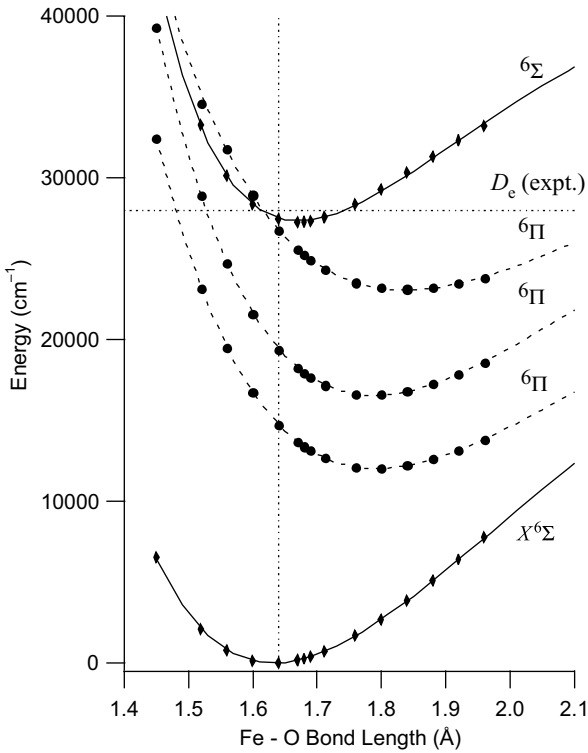


**Figure 6.** Calculated potential energy curves for sextet states of $FeO^+$. The ground electronic state and excited states accessible by allowed electronic transitions from the ground state are shown. Points are calculated using TD–DFT at the B3LYP/6-311G(d,p) level. Solid lines are $\Sigma$ states and dashed lines are $\Pi$ states, the vertical dashed line indicates $r_e$ for the ground state. The experimental value of the dissociation energy $D_e$ is also shown for reference.

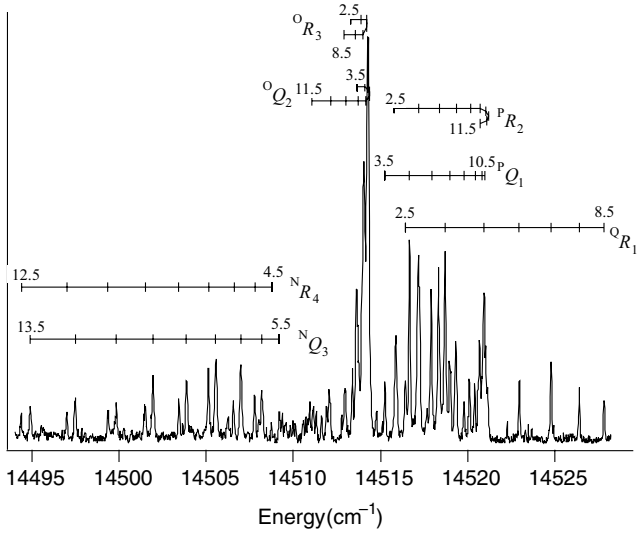


**Figure 7.** Resonance enhanced $(1+1)$ photodissociation spectrum and rotational assignments of the $^6\Pi_{7/2}$ $(v' = 8) \leftarrow {}^6\Sigma$ $(v'' = 0)$ band of $^{56}FeO^+$. Numbers indicate $J''$ for each line; the subscripts indicate the spin component of the $^6\Sigma$ state ($F_1$ is $\Sigma = \frac{5}{2}$); the superscripts indicate $\Delta N$ for the transition.

spectrum. The resolution is limited only by the 0.05 $cm^{-1}$ line width of the laser, leading to clearly resolved rotational structure. Based on the energy shift observed for the minor $^{54}FeO^+$ isotopomer, the transition is from $v'' = 0$ of the $^6\Sigma$ ground state to $v' = 8$ of the $^6\Pi_{7/2}$ excited state. The $^6\Sigma$ ground state has six spin–spin sublevels and we observe transitions from four of them to $v' = 8$, 9 of the $^6\Pi_{7/2}$ excited state. The observed transitions have been fit to a detailed Hamiltonian to obtain rotational constants for the ground and $^6\Pi_{7/2}$ excited states [137]. The rotational constant for the ground state gives $r_0'' = 1.643 \pm 0.001$ Å. Other molecular parameters determined for the $^6\Sigma^+$ ground state are the spin–spin coupling constant $\lambda = -0.126\,cm^{-1}$ and the spin–rotational coupling constant $\gamma = -0.033\,cm^{-1}$. Detailed spectroscopy of $FeO^+$ and similar systems provide a demanding test of electronic structure methods. Measurements of the ground-state bond length and the ground- and excited-state vibrational frequencies test calculations of the potentials, while measurements of the spin–spin and spin–orbit coupling test calculations of the interactions between states. Observation of transitions to high vibrational levels of the $^6\Pi$ state is consistent with the TD–DFT calculations, which predict that the low lying $^6\Pi$ states have charge-transfer character, with much longer bond length than the $^6\Sigma$

ground state. In general, we find that TD–DFT calculations of excited electronic states of open-shell metal-containing diatomics are surprisingly accurate, with mean errors of 0.03 Å in bond lengths, 2000 $cm^{-1}$ in electronic excitation energies and 50 $cm^{-1}$ in vibrational frequencies [137].

### 3. *Photoionization of FeO: Low lying Quartet States of $FeO^+$*

Transition metal containing ions often have low lying electronic states with different spin multiplicity from the ground state. Electronic transitions to these states from the ground state are spin forbidden and often occur at awkward wavelengths, making their study difficult. Photoionization of the neutral provides an alternate route to access these states. For example, electronic structure calculations predict that $FeO^+$ has a $^6\Sigma$ ground state (which our experiments confirm) and several low lying quartet states, $^4\Pi$, $^4\Delta$, and $^4\Phi$ within $\sim$1 eV of the ground state, depending on the level of theory [145, 146, 152, 153]. The quartet states have not been optically observed. All of these states can be accessed by photoionization of neutral FeO ($X$, $^5\Delta$). We have measured photoionization efficiencies for FeO (Fig. 8) and also of CuO at the Advanced Light Source, obtaining ionization energies for the metal oxides with

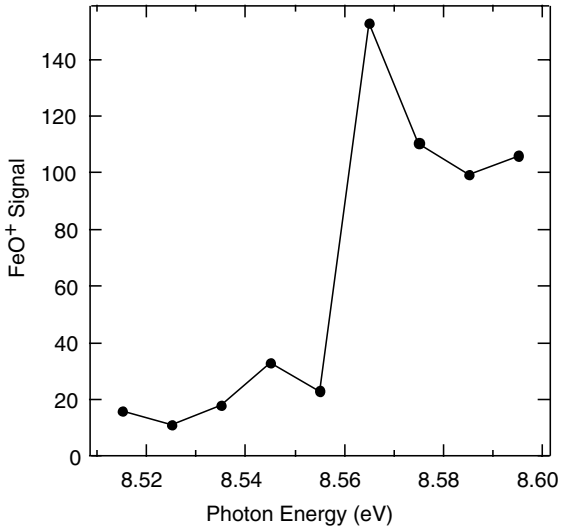


**Figure 8.** Photoionization efficiency curve for $^{56}$FeO near the ionization onset, corresponding to production of $FeO^+$ $X$, $^6\Sigma$.

0.01-eV precision [39]. This allows us to refine the $Fe^+ - O$ bond strength using

$$D_0(M^+{-}O) - D_0(M{-}O) = IE(M) - IE(MO)$$

Recent photofragment imaging experiments give a very precise value $D_0(Fe{-}O) = 4.18 \pm 0.01$ eV [154], which implies $D_0(Fe^+{-}O) = 3.52 \pm 0.02$ eV. This value is consistent with, and slightly more precise than, the guided ion beam value of $3.47 \pm 0.06$ eV [31]. For most transition metal oxides, bond strengths for the ions are significantly more precise than for the neutrals, so measuring the molecule's ionization energy leads to improved values of the neutral bond strength. In this vein, we have also recently measured ionization energies of PtC, PtO, and $PtO_2$.

Photoionization can also access excited electronic states of the ion that are difficult to study by optical methods. The photoionization yield of FeO increases dramatically 0.36 eV above the ionzation energy. This result corresponds to the threshold for producing low spin quartet states of $FeO^+$. These states had not been previously observed, as transitions to them are spin forbidden and occur at inconveniently low energy. Because the $FeO^+ + CH_4$ reaction occurs via low spin intermediates, accurately predicting the energies of high and low spin states is critical.

## C. Spectroscopy of the $[HO{-}Fe{-}CH_3]^+$ Insertion Intermediate

### 1. *Electronic Spectroscopy*

The potential energy surface for the $FeO^+ + CH_4$ reaction has four intermediates: an $[OFe\cdots CH_4]^+$ entrance channel complex, $[HO{-}Fe{-}CH_3]^+$ insertion intermediate and $Fe^+(CH_3OH)$ exit channel complex, as shown in Fig. 4. In addition, there is an $[H_2O{-}Fe{=}CH_2]^+$ exit channel complex that leads to the minor $FeCH_2^+ + H_2O$ channel. As these intermediates are, at least, local minima, once they are produced and cooled, they should be stable in the absence of collisions and they can be studied. Studying these ions is complicated by the fact that they are all isomers and thus cannot be separated in a mass spectrometer. So, we use ion molecule reactions to synthesize a particular intermediate and then characterize it from its photodissociation pathways and photodissociation spectrum. In an elegant series of ICR experiments, Schröder et al. synthesized the intermediates of the $FeO^+ + CH_4$ reaction by reacting $Fe^+$ with a variety of organic precursors. The intermediates were characterized based on fragment ions produced by collision-induced dissociation [46]. Although the reaction conditions in our ion source are very different from those in an ICR, we find that the reactions used by Schröder et al. generally form the same intermediates in our source. We have produced the $[HO{-}Fe{-}CH_3]^+$ and $[H_2O{-}Fe{=}CH_2]^+$

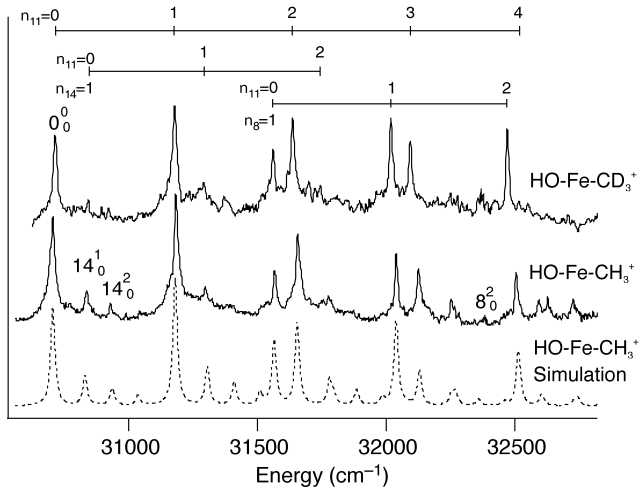


**Figure 9.** Photodissociation spectra of the insertion intermediate of the $FeO^+ + CH_4$ reaction. Top: $[HO{-}Fe{-}CD_3]^+$, middle: $[HO{-}Fe{-}CH_3]^+$, bottom (dashed): Franck–Condon simulation of the $[HO{-}Fe{-}CH_3]^+$ spectrum. The spectrum shows a long progression in the Fe-C stretch ($\nu_{11}' = 478\ cm^{-1}$) and short progressions in the Fe–O stretch ($\nu_8' = 861\ cm^{-1}$) and O–Fe–C bend ($\nu_{14}' = 132\ cm^{-1}$).

intermediates, cooled them in a supersonic expansion, and measured their electronic and vibrational spectra. Here we will focus on the $[HO{-}Fe{-}CH_3]^+$ insertion intermediate, results on $[H_2O{-}Fe{=}CH_2]^+$ have been presented elsewhere [45, 139].

Photodissociation of the insertion intermediate produces $Fe^+ + CH_3OH$ and $FeOH^+ + CH_3$ in a 44:56 ratio at each photodissociation resonance peak. Nonresonant photodissociation leads to less $Fe^+$ product, as shown in Fig. 3. So, in a half-collision experiment, photoexcitation of the $[HO{-}Fe{-}CH_3]^+$ intermediate triggers the $FeO^+ + CH_4$ reaction, leading to the same products as are observed in the bimolecular reaction. The photodissociation spectra of $[HO{-}Fe{-}CH_3]^+$ and $[HO{-}Fe{-}CD_3]^+$ obtained by monitoring $FeOH^+$ are shown in Fig. 9. The data shown was obtained from the insertion intermediate produced by reacting $Fe^+$ with $CH_3OH$ and $CD_3OH$. As this reaction can also produce the $Fe^+(CH_3OH)$ exit channel complex, we also synthesize the ions by reacting $Fe^+$ with acetic acid, which produces $[HO{-}Fe{-}CH_3]^+$ and $[H_2O{-}Fe{=}CH_2]^+$. Monitoring the $Fe^+$ or $FeOH^+$ fragment, we get the same spectrum as shown in Fig. 9, confirming that it is due to the insertion intermediate. If we monitor $FeCH_2^+$, we get a very different photodissociation spectrum due to $[H_2O{-}Fe{=}CH_2]^+$. The spectrum of the insertion intermediate is vibrationally resolved and the peaks show some tailing to lower energy due

to unresolved rotational structure. As these intermediates are probably in the sextet state [45], the peaks are due to vibrations in an electronically excited sextet state of the intermediate. The longest vibrational progression observed is in the Fe—C stretch ($\nu_{11}' = 478\,\mathrm{cm}^{-1}$) and there are short progressions in the Fe—O stretch ($\nu_8' = 861\,\mathrm{cm}^{-1}$) and O—Fe—C bend ($\nu_{14}' = 132\,\mathrm{cm}^{-1}$). This assignment is supported by isotope shifts in the spectrum of $[HO—Fe—CD_3]^+$ and extensive hybrid density functional theory (B3LYP) calculations [45]. The Franck–Condon simulation shown in dashed lines in the figure predicts that electronic excitation leads to a 0.13-Å change in the Fe—C bond length, a 0.05 Å change in the Fe—O bond length, and O—Fe—C angle change of 4°. The low frequency bend is the primary motion required for the molecule to get from the insertion intermediate to transition state TS2. While the electronic spectrum allows us to study an excited electronic state of $[HO—Fe—CH_3]^+$, it gives little information on the structure and bonding in the ground state of the complex. This information is best obtained from vibrational spectroscopy.

### 2. *Vibrational Spectroscopy*

To characterize bonding in the insertion intermediate, we have measured its vibrational spectrum. As noted in Section II, using photofragment spectroscopy to measure vibrational spectra of strongly bound ions is challenging, as one IR photon does not have sufficient energy to break a bond. This is certainly the case for $[HO—Fe—CH_3]^+$, which is bound by $\sim$130 kJ mol$^{-1}$ (three IR photons at 3600 cm$^{-1}$) relative to $Fe^+ + CH_3OH$ [45]. Infrared multiphoton dissociation is inefficient ($<0.1\%$ dissociation at 10 mJ/pulse) and gives a very broad spectrum. Instead, we measure the vibrational spectrum of argon-tagged molecules $[HO—Fe—CH_3]^+(Ar)_n$ ($n = 1,2$) in the O—H stretching region (Fig. 10) [141]. The spectrum of $[HO—Fe—CH_3]^+(Ar)$ peaks at 3646 cm$^{-1}$ and has a shoulder at $\sim$3633 cm$^{-1}$, while the spectrum of $[HO—Fe—CH_3]^+(Ar)_2$ is significantly narrower, peaking at 3660 cm$^{-1}$. For comparison, the O—H stretching frequency in methanol is 3681 cm$^{-1}$. The shoulder in the $[HO—Fe—CH_3]^+(Ar)$ spectrum suggests the presence of two isomers or spin states of the molecule, and this feature persists when we change source conditions. The same spectrum is obtained with methanol and acetic acid as the precursor, confirming that we are studying the insertion intermediate, rather than the exit channel complex. We have extended our previous calculations on the $FeO^+ + CH_4$ reaction to B3LYP and CCSD(T) with larger basis sets, and the calculations predict that the quartet and sextet states of $[HO—Fe—CH_3]^+$ are at very similar energies. Calculations on the argon-tagged complexes predict that the O—H stretching frequency of sextet $[HO—Fe—CH_3]^+$ lies 11 cm$^{-1}$ above that of the quartet state, but that the frequencies are very similar

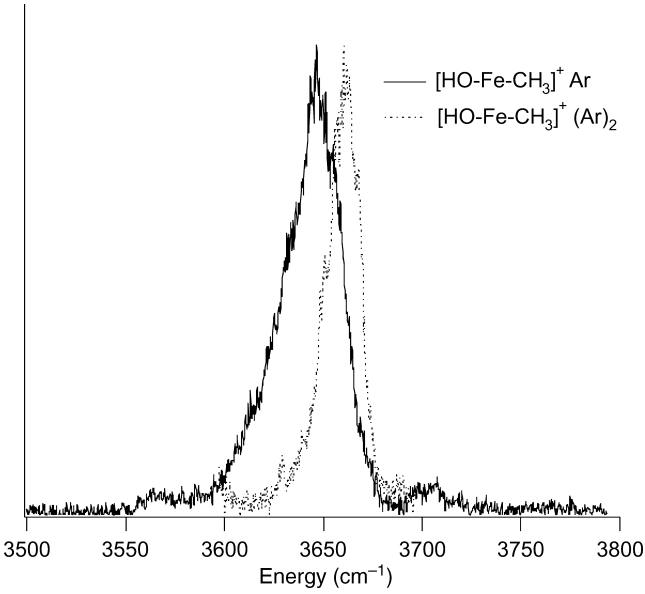


**Figure 10.** Vibrational spectra of the $[HO{-}Fe{-}CH_3]^+$ insertion intermediate in the O–H stretching region. Spectra are obtained by monitoring loss of argon from IR resonance enhanced photodissociation of the argon-tagged complexes $[HO{-}Fe{-}CH_3]^+(Ar)_n$ ($n = 1,2$).

for the argon-tagged complexes. So, it is possible that both the sextet and quartet states of the insertion intermediate are formed in our experiment and that the significant spin–orbit coupling calculated by Shiota and Yoshizawa [144] allows them to interconvert in the source. We have also measured the vibrational spectrum in the C–H stretching region, which is significantly more difficult, as the C–H stretches are at least an order of magnitude weaker than the O–H stretch. We observe peaks at 2880 and 2860 $cm^{-1}$ for $[HO{-}Fe{-}CH_3]^+(Ar)$ and narrower peaks at 2885 and 2860 $cm^{-1}$ for $[HO{-}Fe{-}CH_3]^+(Ar)_2$. The calculations predict these to be the symmetric C–H stretch, which is the most intense and occurs at the lowest energy. They also suggest that the higher frequency vibrations are due to the sextet state. The vibrational spectrum is sensitive to both spin states, as both have intense O–H stretching vibrations. In the electronic photodissociation spectrum, we observe a structured spectrum near 31,000 $cm^{-1}$. The TD-DFT calculations suggest that this is due to the quartet state, as the sextet is not predicted to absorb in this energy region, while the quartet is predicted to have several electronic states with modest absorption from 29,300 to 35,900 $cm^{-1}$. Some of these states also likely lead to the nonresonant photodissociation observed in this region.

## IV. C—O BOND ACTIVATION BY $V^+$: SPECTROSCOPY AND DISSOCIATION DYNAMICS OF $V^+(OCO)_n$

The reaction between $V^+$ cation and $CO_2$ is quite interesting, as it demonstrates the effect of spin on an exothermic reaction, and how spin effects differ between a bimolecular reaction and a photoinduced half-reaction. It also shows how photoexcitation can be used to influence the products of the chemical reaction. The $V^+ + CO_2$ reaction is exothermic:

$$V^+(^5D) + CO_2 \rightarrow VO^+(^3\Sigma) + CO(^1\Sigma) \qquad \Delta H = -52\,\text{kJ mol}^{-1} \qquad (1)$$

However, the reaction does not occur at thermal energies (the reaction rate is $<0.1\%$ of the collision rate) [26], but is observed at higher collision energies [33]. This is unusual: Most exothermic ion molecule reactions have an appreciable rate at thermal energies, as the attractive electrostatic forces between the reactants depress reaction barriers so that they lie below the reactants. Vanadium cation forms an electrostatic entrance channel complex with $CO_2$; calculations show that the complex is linear: $V^+(OCO)$, with a $^5\Delta$ or $^5\Sigma$ ground state [48,155], and guided ion beam experiments [33] show that it is bound by 72 kJ mol$^{-1}$ relative to $V^+ + CO_2$. Collision-induced dissociation [33] of $V^+(OCO)$ leads exclusively to $V^+ + CO_2$ at low energies, with $VO^+$ only observed at collision energies $>$ 8 eV. This result is surprising, as $VO^+$ production is energetically favored, but spin forbidden

$$V^+(OCO) \rightarrow V^+(^5D) + CO_2(^1\Sigma) \qquad \Delta H = 72 \pm 4\,\text{kJ mol}^{-1} \qquad (2a)$$

$$V^+(OCO) \rightarrow VO^+(^3\Sigma) + CO(^1\Sigma) \qquad \Delta H = 20 \pm 10\,\text{kJ mol}^{-1} \qquad (2b)$$

### A. Electronic Spectroscopy of $V^+(OCO)$

Brucat and co-workers studied photodissociation of $V^+(OCO)$ in the visible [156]. The excited-state predissociates, giving a vibrationally resolved spectrum with partially resolved rotational structure with progressions in the $V^+$—OCO stretch and rock, and in the OCO bend. Dissociation occurs via both the reactive $VO^+$ and nonreactive $V^+$ channels, with a $VO^+/V^+$ ratio of 0.4 at the vibronic origin. They also observed interesting mode selectivity in the photodissociation: Exciting the rocking vibration enhances the reactive channel by 50%. Because the reactive channel requires breaking a C—O bond, we felt that the OCO antisymmetric stretch would be similar to the reaction coordinate. So, we proposed that exciting vibronic transitions involving the antisymmetric stretch,

perhaps in combination with $V^+$—OCO stretch and rock, would enhance the reactive channel even further. Brucat and co-workers did not observe bands involving the antisymmetric stretch vibration, presumably due to small Franck–Condon factors. To overcome this problem, we used vibrationally mediated photodissociation to access transitions involving the antisymmetric stretch vibration, $\nu_1$. An IR photon vibrationally excites molecules to $\nu_1'' = 1$, then a visible photon promotes the molecules to vibrational levels in the excited electronic state with $\nu_1' = 1$, whereupon they predissociate, and we measure the products. This experiment would also measure the antisymmetric stretch frequencies in the ground and excited electronic states, which had not been previously determined.

### B. Vibrational Spectroscopy and Vibrationally Mediated Photodissociation

As noted in the experimental section, vibrational predissociation is the simplest way to measure the vibrational spectra of ions. Vibrational predissociation requires that the photon energy exceed the bond strength. The OCO antisymmetric stretch frequency in $V^+(OCO)$ should be similar to the value in bare $CO_2$, 2349 $cm^{-1}$. The $V^+$—OCO bond strength [33] is $6050 \pm 320\,cm^{-1}$, so three IR photons are required to dissociate the molecule, ruling out vibrational predissociation. $V^+(OCO)$ is also a poor candidate for IRMPD studies, as it is small and thus has a low density of vibrational states. We first looked at vibrational spectroscopy of $V^+(OCO)_5$, which had previously been studied by Duncan and co-workers [112]. They find that, for $V^+$, the first four $CO_2$ ligands bind to the metal; additional ligands are in the second solvent shell. This results in weak binding, and our IR resonance enhanced photodissociation spectrum of $V^+(OCO)_5$ is shown in Fig. 11. The antisymmetric stretch vibrational frequency for outer-shell $CO_2$ is nearly unchanged from its value in free $CO_2$. For inner-shell $CO_2$, binding to $V^+$ shifts the antisymmetric stretch 26 $cm^{-1}$ to the blue. This shift should be even larger for the $V^+(OCO)$ cluster, as the metal–ligand interaction is stronger, and Duncan and co-workers observe a peak at 2378 $cm^{-1}$ for the argon-tagged complex $V^+(OCO)Ar$, but the signal for this ion is quite weak [112].

The $V^+(OCO)$ ion has a structured electronic photodissociation spectrum, which allows us to measure its *vibrational* spectrum using vibrationally mediated photodissociation (VMP). This technique requires that the absorption spectrum (or, in our case, the photodissociation spectrum) of vibrationally excited molecules differ from that of vibrationally unexcited molecules. The photodissociation spectrum of $V^+(OCO)$ has an extended progression in the $V^+$—OCO stretch, indicating that the ground and excited electronic states have different equilibrium $V^+$—OCO bond lengths. Thus, the OCO antisymmetric stretch frequency $\nu_1$ should be different in the two states, and the

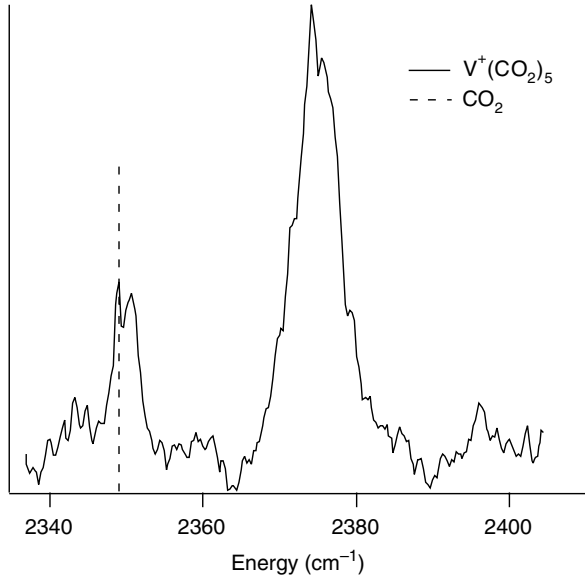


**Figure 11.** Infrared resonance enhanced photodissociation spectrum of $V^+(OCO)_5$ obtained by monitoring loss of $CO_2$. The antisymmetric stretch of outer-shell $CO_2$ is near 2349 $cm^{-1}$ (the value in free $CO_2$, indicated by the dashed vertical line). The vibration shifts to 2375 $cm^{-1}$ for inner-shell $CO_2$.

$\nu_1' = 1 \leftarrow \nu_1'' = 1$ transition will be at a different energy than the $\nu_1' = 0 \leftarrow \nu_1'' = 0$. We use this fact to measure the vibrational spectrum of $V^+(OCO)$ in a *depletion* experiment (Fig. 12a). A visible laser is set to the $\nu_1' = 0 \leftarrow \nu_1'' = 0$ transition at 15,801 $cm^{-1}$, producing fragment ions. A tunable IR laser fires before the visible laser. Absorption of IR photons removes population from the ground state, which is observed as a decrease in the fragment ion signal. This technique is a variation of ion-dip spectroscopy, in which ions produced by $1 + 1$ REMPI are monitored as an IR laser is tuned. Ion-dip spectroscopy has been used by several groups to study vibrations of neutral clusters and biomolecules [157–162].

We observe 8% depletion of the fragment signal at 2391.5 $cm^{-1}$, which establishes the antisymmetric stretch frequency in the $V^+(OCO)$ ground electronic state and that *at least* 8% of the ions are vibrationally excited. This value is only a lower limit because vibrationally excited molecules may also absorb at 15,801 $cm^{-1}$ and photodissociate. The major drawback to the depletion experiment is that we are trying to observe a small decrease in the fragment ion signal, which is not particularly large or stable. Obtaining good signal-to-noise ratio thus requires extensive signal averaging, limiting the number of data points we can measure. An *enhancement* experiment, in

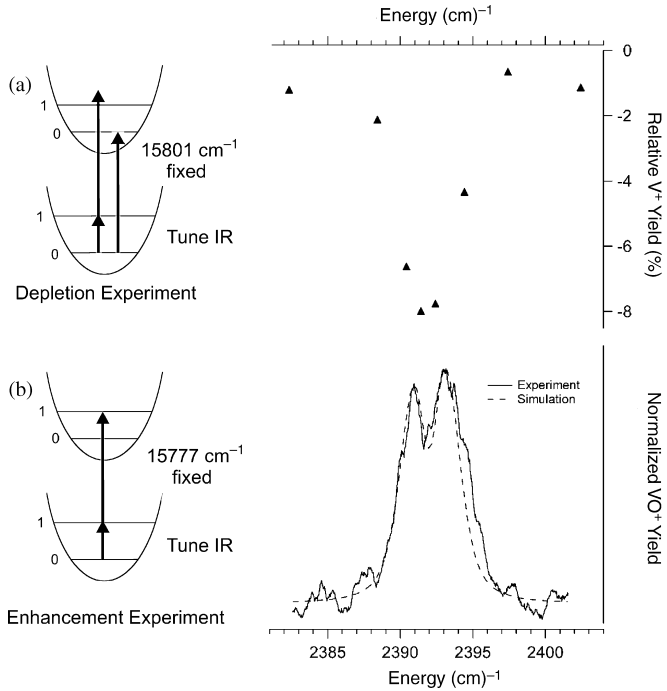


**Figure 12.** Vibrational action spectra of $V^+$(OCO) in the OCO antisymmetric stretch region. (a) Spectrum obtained by monitoring *depletion* in the $V^+$ photofragment produced by irradiation at the vibronic origin at 15,801 $cm^{-1}$. The IR absorption near 2391.5 $cm^{-1}$ removes molecules from $v_1'' = 0$, leading to an 8% reduction in the fragment yield. (b) Spectrum obtained by monitoring *enhancement* in the $VO^+$ photofragment signal as the IR laser is tuned, with the visible laser fixed at 15,777 $cm^{-1}$ (the $v_1' = 1 \leftarrow v_1'' = 1$ transition). The simulated spectrum gives a more precise value of the OCO antisymmetric stretch vibration in $V^+$(OCO) of 2392.0 $cm^{-1}$.

which tuning the IR laser onto a vibrational resonance increases the fragment ion yield from a near-zero background level would greatly improve the signal to noise. In order to do this, we first find a electronic transition originating from $v_1'' = 1$. The IR laser is set to excite the OCO antisymmetric stretch and the visible laser is tuned in the vicinity of the $v_1' = 0 \leftarrow v_1'' = 0$ band. Figure 13 shows that we observe the $v_1' = 1 \leftarrow v_1'' = 1$ band at 15,777 $cm^{-1}$, 24 $cm^{-1}$ to the red of the $0 \leftarrow 0$ band. Now, we can measure the vibrational spectrum with much improved signal-to-noise (and using a much smaller energy spacing) by setting the visible laser to the $v_1' = 1 \leftarrow v_1'' = 1$ electronic transition and tuning the IR laser while monitoring the fragment ion yield. The resulting vibrational action spectrum is shown in Fig. 12(b). The resolution of the spectrum is limited only by the

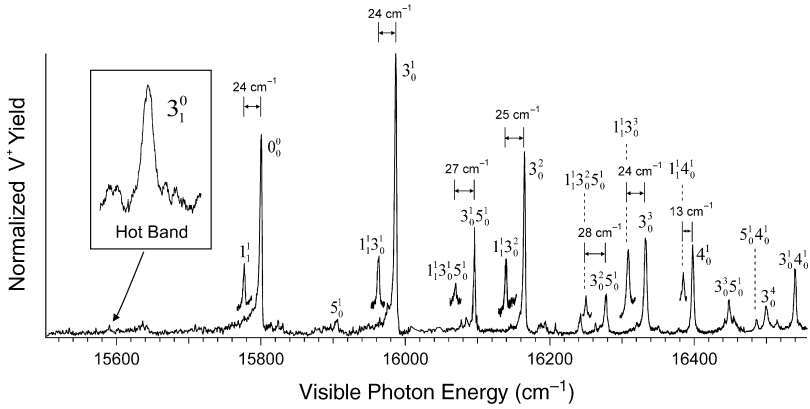


**Figure 13.** Photodissociation spectrum of $V^+(OCO)$, with assignments. Insets and their assignments show the photodissociation spectrum of molecules excited with one quantum of OCO antisymmetric stretch, $\nu_1''$ at 2390.9 $cm^{-1}$. These intensities have been multiplied by a factor of 2. The shifts show that $\nu_1'$ (excited state) lies ~24 $cm^{-1}$ below $\nu_1''$ (ground state), and that there is a small amount of vibrational cross-anharmonicity. The box shows a hot band at 15,591 $cm^{-1}$ that is shifted by 210 $cm^{-1}$ from the origin peak and is assigned to the $V^+$—OCO stretch in the ground state.

IR laser line width. As a result, the spectrum clearly shows P and R branches, establishing that $V^+(OCO)$ is linear. The simulated spectrum (dashed line) gives an improved value for the OCO antisymmetric stretch frequency in the ground electronic state $\nu_1'' = 2392.0\ cm^{-1}$. The simulation assumes a $^5\Sigma$ ground state and uses $B'' = B' = 0.057\ cm^{-1}$, the value given by our density functional theory calculations [48]. Because the rotational constants are so small, the simulated spectrum is not sensitive to B′ or B″, but B′—B″ affects the relative intensities of the P and R branches, and the separation between the branches is due to the 12 K rotational temperature of the ions. This is the first use of vibrationally mediated photodissociation for spectroscopy of an ion. The $\nu_1' = 1 \leftarrow \nu_1'' = 1$ band lies 24 $cm^{-1}$ below $\nu_1' = 0 \leftarrow \nu_1'' = 0$, so the OCO antisymmetric stretch frequency in the excited electronic state is $\nu_1{}' = 2392–24 = 2368\ cm^{-1}$. Table I summarizes the vibrational frequencies of the ground and excited states of $V^+(OCO)$ and compares the values to those in $CO_2$. Electronic excitation of $V^+(OCO)$ lengthens the metal–ligand bond, resulting in a smaller blue shift. More generally, based on our calculations [163], the blue shift in the OCO antisymmetric stretch on binding to $V^+$ correlates with the amount of charge transferred to the $CO_2$, which means that this is an electronic effect, rather than simply a mechanical effect due to the proximity of the $V^+$ to the ligand. Larger $V^+(OCO)_n$ clusters have smaller blue shifts [112], due to longer metal–ligand bonds and less charge transfer to each ligand.

TABLE I
Vibrational Frequencies ($cm^{-1}$) of $V^+(OCO)$ and $CO_2$

| | $\nu_1$ OCO Antisymmetric Stretch | $\nu_2$ OCO Symmetric Stretch | $\nu_3$ Stretch $V^+$—(OCO) | $\nu_4$ OCO Bend | $\nu_5$ $V^+$—(OCO) Rock |
|---|---|---|---|---|---|
| $V^+(OCO)$ Ground State | 2392.0 | | 210 | | |
| $V^+(OCO)$ [15.8] State (Visible) | 2368 | 1340 | 186 | 597 | 105 |
| $CO_2$ | 2349.16 | 1333 | | 667.38 | |

## C. Mode Selective Photodissociation of $V^+(OCO)$

Figure 13 shows the photodissociation spectrum of $V^+(OCO)$ in the visible and the insets show the photodissociation spectrum of vibrationally excited molecules containing one quantum of OCO antisymmetric stretch ($\nu_1$). The shift between a vibronic band and the corresponding $\nu_1' = 1 \leftarrow \nu_1'' = 1$ sequence band is $\sim$24 $cm^{-1}$ in each case, indicating that there is little cross-anharmonicity between $\nu_1$ and the other vibrations observed. To characterize how the OCO antisymmetric stretch, OCO bend and metal–ligand stretch and rock affect the products of photodissociation of $V^+(OCO)$, we used difference spectra to measure the relative yield of the nonreactive $V^+$ (and $CO_2$) versus the reactive $VO^+$ (and CO) channels at each band assigned in Fig. 13. The results, shown in Fig. 14, indicate that there is mode selectivity in the reaction. Data $<$ 16,600 $cm^{-1}$ was obtained from one-photon dissociation. Compared to the origin band, one quantum of $V^+$—(OCO) rock ($\nu_5'$) enhances the reactive channel, while one quantum of $V^+$—(OCO) stretch ($\nu_3'$) or $CO_2$ bend ($\nu_4'$) slightly decreases it. These results agree with those previously obtained by Brucat and co-workers [156]. We also find that exciting $3\nu_3' + \nu_5'$ enhances reactivity by $\sim$70%, a result that was not reported earlier, presumably due to the low total dissociation yield for this peak. Brucat and co-workers also observed vibronic features at 17,000–17,500 $cm^{-1}$ that lead to $VO^+/V^+$ branching ratios of $\sim$1.2, showing a trend toward higher $VO^+$ production at higher energy. We used vibrationally mediated photodissociation to measure how the OCO antisymmetric stretch vibration $\nu_1$, alone or in combination with other vibrations, affects the mode selectivity. We excite the peak of the P branch of $\nu_1$ at 2390.9 $cm^{-1}$, and then photoexcite vibrationally excited molecules in the visible. The $VO^+/V^+$ branching ratio for these vibronic transitions is shown in the high energy portion of Fig. 14, where the energy is the total energy of the IR and

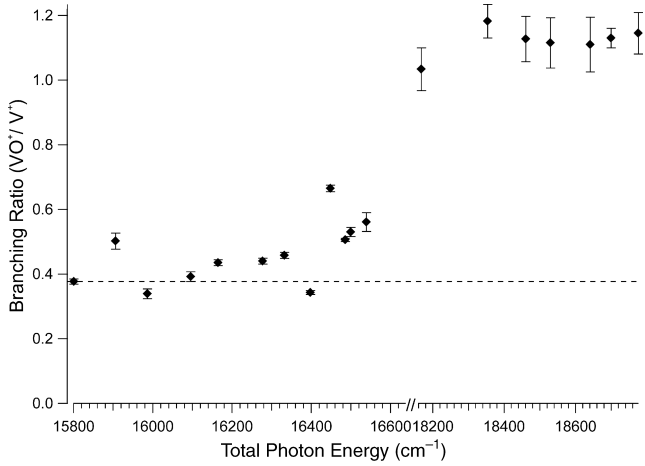


**Figure 14.** Mode selectivity in photodissociation of $V^+$(OCO). The ratio of the reactive ($VO^+ + CO$) to nonreactive ($V^+ + CO_2$) product is measured at the peaks of the vibronic bands labeled in Fig. 13. The data below 16,600 $cm^{-1}$ is from bands accessed by one-photon excitation; data at higher energy was obtained by vibrationally mediated photodissociation exciting the OCO antisymmetric stretch.

visible photons. Exciting the OCO antisymmetric stretch enhances the reactive channel by almost a factor of 3. Exciting combination bands of the antisymmetric stretch with several other vibrations further increases the $VO^+$ yield slightly, but combination bands involving the antisymmetric stretch all give similar branching ratios [163].

The photodissociation and guided ion beam experiments on $V^+$(OCO) give interesting and, at first glance, conflicting results. Photodissociation of $V^+$(OCO) leads to significant amounts of the reactive, spin forbidden $VO^+$ product, and its yield increases significantly for specific vibrations in the excited electronic state [156, 163]. On the other hand, collision-induced dissociation of $V^+$(OCO) at energies $< 8$ eV leads exclusively to spin-allowed $V^+$ [33]. We also find that photodissociation in the near IR, near 7000 $cm^{-1}$ only produces $V^+$ [163]. To investigate these observations, we carried out extensive electronic structure calculations. We first characterized the stationary points on the $V^+ + CO_2$ potential energy surface (Fig. 15). The ground state of $V^+$ is high spin ($^5D$), and the ground state of the $V^+$(OCO) complex is also a quintet. Triplet $OV^+$(CO) is the most stable species on the potential energy surface, so insertion of $V^+$ into the C—O bond is exothermic. However, there is a substantial barrier to insertion, that explains why the $V^+ + CO_2 \rightarrow VO^+ + CO$ reaction does not occur at thermal energies [26]. The transition state to insertion is tight and quite bent. So, in collision-induced dissociation of $V^+$(OCO), the

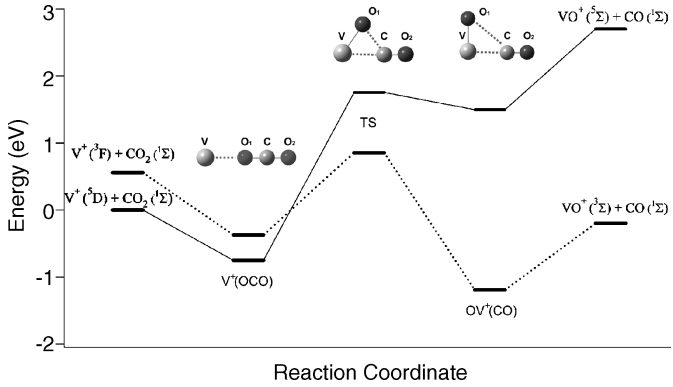


**Figure 15.** Calculated potential energy surface and geometries of intermediates of the $V^+ + CO_2$ reaction. The energy of the lowest energy state for the quintet (solid lines) and triplet (dotted lines) stationary points are shown. Energies are calculated at the CCSD(T)/6-311+G(3df) level, at the B3LYP/6-311+G(d) geometry and include zero-point energy at the B3LYP/6-311+G(d) level.

$V^+ + CO_2$ channel dominates as it is spin allowed and occurs via a loose transition state. In contrast, production of $VO^+$ is spin forbidden and goes *via* a tight transition state that lies higher in energy than $V^+ + CO_2$.

Interpreting the photodissociation experiments requires further calculations to characterize the ground and excited triplet and quintet states of $V^+$(OCO), and the spin–orbit coupling between the states. We find that there are several triplet states that cross the excited quintet states accessed in the photodissociation experiments. These crossings occur at bent $V^+$—OCO geometries and extended $V^+$—OCO bond lengths. Also, the excited quintet states have modest spin–orbit couplings of $\lesssim 90\,cm^{-1}$ to nearby triplet states [163]. These observations help to explain the photodissociation results. The photodissociation spectrum of $V^+$(OCO) in the near-IR is broad and poorly resolved [48], suggesting that dissociation is rapid. This gives little time for the excited quintet state to convert to triplet states, so quintet $V^+$ is the only channel observed.

In contrast, the photodissociation spectrum of $V^+$(OCO) in the visible shows vibrational and partial rotational structure. The observed $< 3.5\,cm^{-1}$ line width, indicates excited state lifetimes of at least 1.4 ps. During this time, the molecules have an opportunity to cross to triplet surfaces, from which they can dissociate to form $VO^+$ ($^3\Sigma$). The calculations also help to explain the observed mode selectivity. Exciting vibrations that lead to regions of the excited state potential with higher spin–orbit coupling should enhance production of $VO^+$. Triplet states of $V^+$(OCO) cross the excited quintet state at long $V^+$—OCO bond lengths and at large $V^+$—OCO bend angles. Thus, exciting the $V^+$—OCO stretch ($\nu_3'$) and the $V^+$—OCO rock ($\nu_5'$) should enhance $VO^+$ production, as is

observed. We also find that exciting the OCO antisymmetric stretch $\nu_1'$ leads to significant increase in the $VO^+$ product. If $V^+(OCO)$ dissociated to produce $VO^+ + CO$ via a spin-allowed, collinear transition state, then the OCO antisymmetric stretch would be similar to the reaction coordinate, and exciting $\nu_1'$ should enhance $VO^+$ production. The calculations suggest that the reaction mechanism is much more complex: The transition states leading to $VO^+$ are not linear, and second, producing $VO^+$ requires intersystem crossing to the triplet surface, which is enhanced at nonlinear geometries. Thus, the enhanced reactivity we observe following excitation of the OCO antisymmetric stretch is likely due to overall enhancement of $VO^+$ production with increasing energy, combined with a mode selective effect due to stretching the C—O bond, which is required for reaction, even at nonlinear geometries.

## V. PREREACTIVE COMPLEXES: VIBRATIONAL SPECTROSCOPY OF $Fe^+(CH_4)_n$

Most of the third-row transition metal cations react with methane under thermal conditions to produce $MCH_2^+ + H_2$ [164]. The corresponding reactions of first- and second-row $M^+$ are endothermic [18]. Even in these cases, bonding in $M^+(CH_4)$ is not merely electrostatic, but includes significant covalency due to donation from C—H bonding orbitals into empty or partially empty 4*s* and 3*d* orbitals on the metal, along with back donation into C—H antibonding orbitals. These interactions weaken the C—H bonds and significantly lower the C—H stretching frequencies, so vibrational spectroscopy of $M^+(CH_4)_n$ entrance channel complexes reveals the amount of donation and backdonation. For our first studies [165] of vibrational spectroscopy of these complexes we selected $Fe^+(CH_4)_n$. The complexes are easy to produce, and the $Fe^+ + CH_4$ reaction is 123-kJ $mol^{-1}$ endothermic [31, 63, 166], and there is a substantial barrier to C—H insertion [167] so, at the conditions in our ion source, we should only produce the entrance channel complex. Later studies will look at vibrational spectra of the entrance channel complex of the exothermic $FeO^+ + CH_4$ reaction, which is more challenging to produce.

Sequential binding energies of methane to $Fe^+$ have been measured by Schultz and Armentrout using collision-induced dissociation [168] and more recently by Zhang, Kemper, and Bowers by cluster equilibrium [169]. According to the equilibrium measurements, the first methane binds by 77 kJ $mol^{-1}$ and the second binds by 108 kJ $mol^{-1}$. Stronger binding of the second ligand is often observed in electrostatic $Fe^+$ complexes. The first excited state of $Fe^+$ ($3d^7$, $^4$F) interacts more strongly with ligands than the $^6$D ($3d^6\,4s$) ground state, as the 4*s* orbital is empty, reducing repulsive interactions. Calculations predict that $Fe^+(CH_4)$ has a quartet ground state [169], so its measured binding energy includes the 24 kJ $mol^{-1}$ $Fe^+$ $^6$D—$^4$F promotion energy. Larger clusters (at least up to $n = 6$) are calculated to

remain quartets, so this promotion energy is no longer an issue. Binding energies for the third and fourth methane are much smaller, 23 and 20 kJ mol$^{-1}$. This large change in binding energy with cluster size suggests that the binding in these complexes is not simply electrostatic. We measured the resonance enhanced dissociation spectra of $Fe^+(CH_4)_n$ ($n = 3,4$) in the C—H stretching region (Fig. 16). The $CH_4$ binding energies are sufficiently small that absorption of one

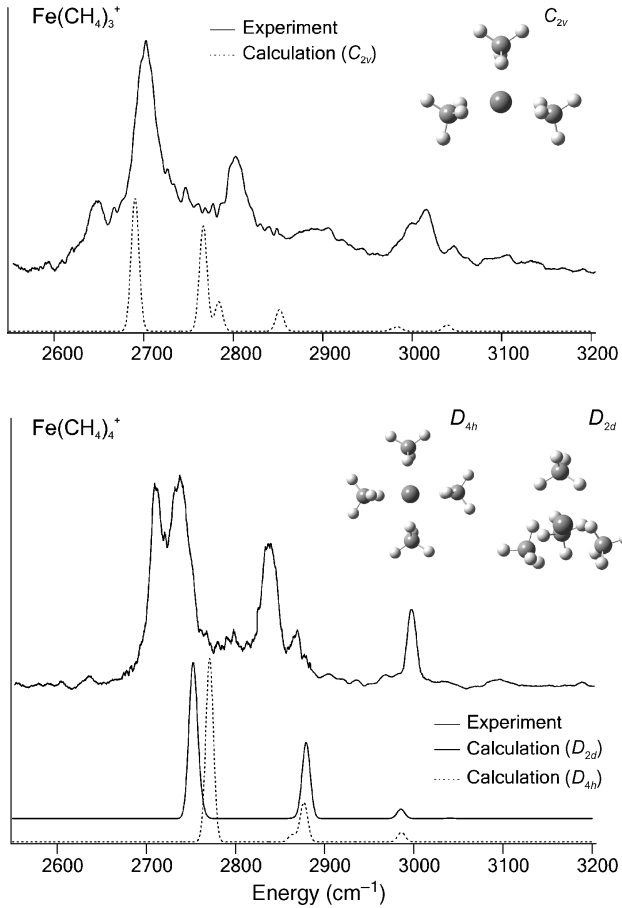


**Figure 16.** Experimental and calculated IR resonance enhanced photodissociation spectra of $Fe^+(CH_4)_3$ and $Fe^+(CH_4)_4$. Experimental spectra were obtained by monitoring loss of $CH_4$. Calculated spectra are based on vibrational frequencies and intensities calculated at the B3LYP/6-311+G(d,p) level. Calculated frequencies are scaled by 0.96. The calculated spectra have been convoluted with a 10-cm$^{-1}$ full width at half-maximum (FWHM) Gaussian. The $D_{2d}$ and $D_{4h}$ geometries of $Fe^+(CH_4)_4$ are calculated to have very similar energies, and it appears that both isomers are observed in the experiment.

IR photon leads to dissociation. The $Fe^+(CH_4)_3$ cluster has an intense absorption at 2703 $cm^{-1}$, with smaller peaks at 2648, 2803, 2895, and 3015 $cm^{-1}$. Compared to the C—H stretching frequencies in bare $CH_4$ (2917-$cm^{-1}$ symmetric stretch and 3019-$cm^{-1}$ antisymmetric stretch), the large peak is red-shifted $> 200\,cm^{-1}$. The red shift is smaller in the $Fe^+(CH_4)_4$ cluster, which has a doublet at 2711/2737 $cm^{-1}$ and large peaks at 2838 and 2998 $cm^{-1}$. Zhang et al. calculated structures of low lying isomers of $Fe^+(CH_4)_n$ and their binding energies using the B3LYP method with the 6-31G(d,p) basis on carbon and hydrogen and the TZVP and augmented Wachter's basis on iron [169]. For several of the clusters they identify multiple isomers with similar calculated energies, with the energy difference depending on the basis set. In principle, the supersonic expansion in our experiment should cool the molecules to the minimum-energy structure, so to identify this structure we compare measured and calculated vibrational spectra. Thus, we reoptimized the geometries and calculated energies and vibrational frequencies and intensities at the B3LYP/6-311+G(d,p) level. Calculated frequencies have been scaled by 0.96, which predicts C—H stretching frequencies for $CH_4$ within 15 $cm^{-1}$ of experiment. Due to the high symmetry of the complexes, the calculated vibrational spectra consist of only a few peaks. The calculated spectrum for $Fe^+(CH_4)_3$ is in good agreement with experiment, although it does not reproduce the smaller peak at 2648 $cm^{-1}$. This may be due to an isomer in which one of the methanes is even closer to the metal. For the larger $Fe^+(CH_4)_4$ cluster, neither of the low energy isomers has a calculated vibrational spectrum with a doublet near 2700 $cm^{-1}$. However, the calculations reproduce the doublet observed at 2711/2737 $cm^{-1}$ if both the $D_{2d}$ and $D_{4h}$ isomers are included. Our calculations predict that the $D_{4h}$ isomer is more stable by a mere 21 $cm^{-1}$, so the presence of two isomers in the beam is not unreasonable.

The calculated C—H stretching frequencies are very sensitive to the C—H bond lengths, which in turn depend on the metal–methane distance. In $Fe^+(CH_4)_3$ each methane is bound to the metal in a $\eta_2$ configuration. The calculated C—H bond length $r_{CH}$ is 1.114 Å for hydrogens pointing toward the metal, 0.023 Å longer than in bare $CH_4$, while $r_{CH} = 1.089$ Å for the hydrogens pointing away from the metal. In $Fe^+(CH_4)_4$ the $D_{4h}$ structure has four equal Fe—C bond lengths, with the proximate C—H bonds extended by 0.017 Å. The $D_{2d}$ isomer has two short and two longer Fe—C distances; the C—H bonds are extended by 0.019 Å for the nearer methanes. Zhang et al. note that systematic measurements for many metals, along with theoretical studies, were required to establish the relative importance of four factors to binding of $M^+$ to $H_2$ [169]. These are donation from bonding orbitals on the ligand to empty 4*s* and partially empty 3*d* orbitals on the metal, backdonation from partially filled 3*d* orbitals to $\sigma^*$ orbitals on the ligand, metal–ligand repulsion due to partially filled 3*d* and 4*s* orbitals, and simple electrostatic attraction. Systematic studies of the vibrational spectroscopy of $M^+(CH_4)_n$, along

with thermodynamic measurements, should allow us to characterize metal–methane bonding in even greater detail.

## VI. FUTURE PROSPECTS

Characterizing the potential energy surfaces of an ion molecule reaction requires using a variety of experimental techniques. The studies described above use vibrational and electronic spectroscopy as well as photoelectron spectroscopy, each of which is sensitive to particular features of the potential. Advances in techniques and equipment are extending the applicability of each of these techniques. Our current IR laser system is limited to the range of 2100 to $>4000\,cm^{-1}$. Free electron lasers have a much broader tunability down to $\sim 600\,cm^{-1}$ and outstanding fluences, but they have modest line width and beam time on these multiuser facilities is limited. Difference frequency mixing in the new nonlinear optical materials $LiInS_2$ and $AgGaSe_2$ is extending the tunability of laboratory infrared lasers down to 900 and $600\,cm^{-1}$, respectively [170]. This region of the IR spectrum has recently been used in elegant laboratory studies of vibrational spectra and structure of $H_3O^+(H_2O)_n$ [79, 80]. Using $AgGaSe_2$ to obtain light at these longer wavelengths will allow us to directly probe M—OH and $M{=}CH_2$ stretches, as well as C=C and C=O stretches and H—C—H bends, which are beyond the tuning range of our current IR laser. Improved techniques for vibrational photofragment spectroscopy will also extend the systems that can be studied. Techniques to measure the vibrational spectra of unperturbed ions with $<1\text{-}cm^{-1}$ resolution are particularly attractive. Vibrationally mediated photodissociation is one such method, and we are exploring complementary methods.

Photoelectron spectroscopy of negative ions has been used to probe the transition state of neutral reactions [16, 17], so photoelectron spectroscopy of appropriate neutral complexes could be a powerful tool for studying the potential energy surfaces of reactions of transition metal cations. As discussed above, we have measured photoionization efficiencies of FeO, CuO, PtC, PtO, and $PtO_2$ at the Chemical Dynamics beamline at the Advanced Light Source. We have also obtained preliminary photoelectron spectra of FeO. These photoelectron imaging experiments are significantly more challenging as the source has to produce good yields of the neutral of interest, with excellent selectivity. Photoelectrons from other neutrals can obscure features from the molecule of interest. Photoelectron–photoion coincidence experiments eliminate most interferences, but have far lower signal. Yang and co-workers have elegantly applied ZEKE photoelectron spectroscopy to studying metal–ligand complexes with ionization energies $<\sim 6$ eV [171]. Covalently bound complexes of late transition metal ions tend to have ionization energies $>8$ eV, in the vacuum UV, where current laboratory laser systems have much

lower fluences. A possible solution to this problem is resonant multiphoton ionization, where the resonance selects the neutral of interest, and all photon energies lie $<6$ eV [172, 173].

Studying photoelectron spectroscopy of intermediates of metal ion reactions requires synthesizing neutrals with a geometry similar to the ion of interest. Several third-row transition metal cations react with methane at thermal energies, but no neutral metal atoms do. However, calculations show that neutral Pt readily inserts into the C—H bond in methane, producing a H—Pt—$CH_3$ intermediate that lies 1.4 eV below the reactants [174]. It is fairly long lived, which leads to the observed high termolecular rate for the Pt + $CH_4$ clustering reaction [174–176]. We plan to measure the photoionization of H—Pt—$CH_3$, which would give the energy of this insertion intermediate relative to Pt + $CH_4$, as the corresponding value has been measured for the cation [35]. Subsequent photoelectron spectroscopy of H—Pt—$CH_3$ would measure vibrational frequencies of $[H—Pt—CH_3]^+$, particularly the Pt—C stretch, complementing vibrational spectroscopy, which is better suited to higher frequency vibrations.

## Acknowledgments

Financial support from the National Science Foundation under award numbers CHE-0308439 and CHE-0608446 is gratefully acknowledged. The photofragment studies described in this chapter are the work of many talented group members: graduate students Fernando Aguirre, Gokhan Altinay, Murat Citir, John Husband, Kay Stringer and Chris Thompson and undergraduate Peter Ferguson. Photoionization experiments at the Advanced Light Source (ALS) were carried out with the expert assistance of Drs. Musahid Ahmed, Dr. Johannes Abate, Dr. Leonid Belau, and Dr. Christophe Nicolas and Prof. Stephen Leone. The Chemical Dynamics beamline at the ALS is supported by the Director of the Office of Energy Research, Office of Basic Energy Sciences, Chemical Sciences Division of the U. S. Department of Energy under Contract No. DE-AC02-05CH11231.

## References

1. R. D. Levine and R. B. Bernstein, *Molecular Reaction Dynamics and Chemical Reactivity.* Oxford University Press, New York, 1987.
2. P. R. Brooks, *Chem. Rev.* **88**, 407 (1988).
3. M. D. Barnes, P. R. Brooks, R. F. Curl, P. W. Harland, and B. R. Johnson, *J. Chem. Phys.* **96**, 3559 (1992).
4. P. D. Kleiber, W. C. Stwalley, and K. M. Sando, *Annu. Rev. Phys. Chem.* **44**, 13 (1993).
5. J. C. Polanyi and A. H. Zewail, *Acc. Chem. Res.* **28**, 119 (1995).
6. A. H. Zewail, *J. Phys. Chem.* **100**, 12701 (1996).
7. A. J. Hudson, H. B. Oh, J. C. Polanyi, and P. Piecuch, *J. Chem. Phys.* **113**, 9897 (2000).
8. A. Keller, R. Lawruszczuk, B. Soep, and J. P. Visticot, *J. Chem. Phys.* **105**, 4556 (1996).
9. J. M. Mestdagh, B. Soep, M. A. Gaveau, and J. P. Visticot, *Int. Rev. Phys. Chem.* **22**, 285 (2003).
10. P. D. Kleiber and J. Chen, *Int. Rev. Phys. Chem.* **17**, 1 (1998).
11. W. Y. Lu, T. H. Wong, and P. D. Kleiber, *Chem. Phys. Lett.* **347**, 183 (2001).
12. W. Y. Lu, Y. Abate, T. H. Wong, and P. D. Kleiber, *J. Phys. Chem. A* **108**, 10661 (2004).

13. W.-Y. Lu, P. D. Kleiber, M. A. Young, and K.-H. Yang, *J. Chem. Phys.* **115**, 5823 (2001).
14. C. R. Moylan, J. A. Dodd, C. C. Han, and J. I. Brauman, *J. Chem. Phys.* **86**, 5350 (1987).
15. K. M. Ervin, J. Ho, and W. C. Lineberger, *J. Chem. Phys.* **91**, 5974 (1989).
16. R. B. Metz, S. E. Bradforth, and D. M. Neumark, *Adv. Chem. Phys.* **81**, 1 (1992).
17. D. M. Neumark, *Phys. Chem. Chem. Phys.* **7**, 433 (2005).
18. K. Eller and H. Schwarz, *Chem. Rev.* **91**, 1121 (1991).
19. J. C. Weisshaar, *Acc. Chem. Res.* **26**, 213 (1993).
20. P. B. Armentrout, in *Organometallic Bonding and Reactivity: Fundamental Studies*, J. M. Brown and P. Hofmann (eds.), Springer-Verlag, Berlin, 1999, vol. IV, pp. 1–45.
21. D. Schröder and H. Schwarz, *Angew. Chem. Intl. Ed. Engl.* **29**, 1433 (1990).
22. D. Schröder and H. Schwarz, *Helv. Chim. Acta* **75**, 1281 (1992).
23. D. Schröder, H. Schwarz, and S. Shaik, *Struct. Bonding* **97**, 91 (2000).
24. D. K. Böhme and H. Schwarz, *Angew. Chem., Int. Ed. Engl.* **44**, 2336 (2005).
25. R. B. Metz, *Int. Rev. Phys. Chem.* **23**, 79 (2004).
26. G. K. Koyanagi and D. K. Bohme, *J. Phys. Chem. A* **110**, 1232 (2006).
27. S. S. Yi, M. R. A. Blomberg, P. E. M. Siegbahn, and J. C. Weisshaar, *J. Phys. Chem. A* **102**, 395 (1998).
28. R. J. Noll, S. S. Yi, and J. C. Weisshaar, *J. Phys. Chem. A* **102**, 386 (1998).
29. E. L. Reichert, S. S. Yi, and J. C. Weisshaar, *Int. J. Mass. Spectrom.* **196**, 55 (2000).
30. K. M. Ervin, *Chem. Rev.* **101**, 391 (2001).
31. P. B. Armentrout and B. L. Kickel, in *Organometallic Ion Chemistry*, B. S. Freiser (ed.), Kluwer Academic Publishers, Dordrecht, The Netherlands, 1996, p. 1.
32. P. B. Armentrout, *Int. J. Mass Spectrom.* **227**, 289 (2003).
33. M. R. Sievers and P. B. Armentrout, *J. Chem. Phys.* **102**, 754 (1995).
34. C. L. Haynes, Y. M. Chen, and P. B. Armentrout, *J. Phys. Chem.* **100**, 111 (1996).
35. X. G. Zhang, R. Liyanage, and P. B. Armentrout, *J. Am. Chem. Soc.* **123**, 5563 (2001).
36. P. B. Armentrout, *Ann. Rev. Phys. Chem.* **41**, 313 (1990).
37. L. Sanders, S. D. Hanton, and J. C. Weisshaar, *J. Chem. Phys.* **92**, 3498 (1990).
38. H. Schwarz, *Int. J. Mass Spectrom.* **237**, 75 (2004).
39. R. B. Metz, C. Nicolas, M. Ahmed, and S. R. Leone, *J. Chem. Phys.* **123**, 114313 (2005).
40. T. G. Dietz, M. A. Duncan, D. E. Powers, and R. E. Smalley, *J. Chem. Phys.* **74**, 6511 (1981).
41. P. J. Brucat, L.-S. Zheng, C. L. Pettiette, S. Yang, and R. E. Smalley, *J. Chem. Phys.* **84**, 3078 (1986).
42. D. Proch and T. Trickl, *Rev. Sci. Instrum.* **60**, 713 (1989).
43. *Organometallic Ion Chemistry*, B. S. Freiser (ed.), Kluwer Academic Publishers, Dordrecht, The Netherlands, 1996.
44. R. L. Hettich and B. S. Freiser, *J. Am. Chem. Soc.* **108**, 2537 (1986).
45. F. Aguirre, J. Husband, C. J. Thompson, K. L. Stringer, and R. B. Metz, *J. Chem. Phys.* **116**, 4071 (2002).
46. D. Schröder, A. Fiedler, J. Hrusák, and H. Schwarz, *J. Am. Chem. Soc.* **114**, 1215 (1992).
47. J. Husband, F. Aguirre, P. Ferguson, and R. B. Metz, *J. Chem. Phys.* **111**, 1433 (1999).
48. M. Citir, G. Altinay, and R. B. Metz, *J. Phys. Chem. A* **110**, 5051 (2006).

49. A. Kamariotis, T. Hayes, D. Bellert, and P. J. Brucat, *Chem. Phys. Lett.* **316**, 60 (2000).
50. W. C. Wiley and I. H. McLaren, *Rev. Sci. Instrum.* **26**, 1150 (1955).
51. L. A. Posey, M. J. DeLuca, and M. A. Johnson, *Chem. Phys. Lett.* **131**, 170 (1986).
52. R. E. Continetti, D. R. Cyr, and D. M. Neumark, *Rev. Sci. Instrum.* **63**, 1840 (1992).
53. D. S. Cornett, M. Peschke, K. Laitting, P. Y. Cheng, K. F. Willey, and M. A. Duncan, *Rev. Sci. Instrum.* **63**, 2177 (1992).
54. V. I. Karataev, B. A. Mamyrin, and D. V. Shmikk, *Sov. Phys.-Tech. Phys.* **16**, 1177 (1972).
55. B. A. Mamyrin, V. I. Karataev, D. V. Shmikk, and V. A. Zagulin, *Sov. Phys.-JETP* **37**, 45 (1973).
56. C. J. Thompson, J. Husband, F. Aguirre, and R. B. Metz, *J. Phys. Chem. A* **104**, 8155 (2000).
57. K. P. Faherty, C. J. Thompson, F. Aguirre, J. Michne, and R. B. Metz, *J. Phys. Chem. A* **105**, 10054 (2001).
58. C. J. Thompson, K. P. Faherty, K. L. Stringer, and R. B. Metz, *Phys. Chem. Chem. Phys.* **7**, 814 (2005).
59. K. L. Stringer, M. Citir, and R. B. Metz, to be submitted (2008).
60. J. W. Buchanan, J. E. Reddic, G. A. Grieves, and M. A. Duncan, *J. Phys. Chem. A* **102**, 6390 (1998).
61. R. L. Hettich, T. C. Jackson, E. M. Stanko, and B. S. Freiser, *J. Am. Chem. Soc.* **108**, 5086 (1986).
62. L. M. Russon, S. A. Heidecke, M. K. Birke, J. Conceicao, M. D. Morse, and P. B. Armentrout, *J. Chem. Phys.* **100**, 4747 (1994).
63. J. Husband, F. Aguirre, C. J. Thompson, C. M. Laperle, and R. B. Metz, *J. Phys. Chem. A* **104**, 2020 (2000).
64. J. Husband, F. Aguirre, C. J. Thompson, and R. B. Metz, *Chem. Phys. Lett.* **342**, 75 (2001).
65. D. Lessen and P. J. Brucat, *J. Chem. Phys.* **91**, 4522 (1989).
66. D. Lessen, R. L. Asher, and P. Brucat, *Int. J. Mass Spec. Ion. Proc.* **102**, 331 (1990).
67. R. L. Asher, D. Bellert, T. Buthelezi, and P. J. Brucat, *Chem. Phys. Lett.* **227**, 277 (1994).
68. C. J. Thompson, K. L. Stringer, M. McWilliams, and R. B. Metz, *Chem. Phys. Lett.* **376**, 588 (2003).
69. K. L. Stringer, M. Citir, and R. B. Metz, *J. Phys. Chem. A* **108**, 6996 (2004).
70. D. Bellert, T. Buthelezi, V. Lewis, K. Dezfulian, D. Reed, T. Hayes, and P. J. Brucat, *Chem. Phys. Lett.* **256**, 555 (1996).
71. D. Bellert, T. Buthelezi, T. Hayes, and P. J. Brucat, *Chem. Phys. Lett.* **276**, 242 (1997).
72. K. M. Gunawardhana and R. B. Metz, to be submitted (2008).
73. M. A. Duncan, *Int. Rev. Phys. Chem.* **22**, 407 (2003).
74. M. A. Duncan, *Int. J. Mass Spectrom.* **200**, 545 (2000).
75. R. S. Walters, P. R. von Schleyer, C. Corminboeuf, and M. A. Duncan, *J. Am. Chem. Soc.* **127**, 1100 (2005).
76. N. R. Walker, R. S. Walters, G. A. Grieves, and M. A. Duncan, *J. Chem. Phys.* **121**, 10498 (2004).
77. G. Gregoire, J. Velasquez, and M. A. Duncan, *Chem. Phys. Lett.* **349**, 451 (2001).
78. E. A. Woronowicz, W. H. Robertson, G. H. Weddle, M. A. Johnson, E. M. Myshakin, and K. D. Jordan, *J. Phys. Chem. A* **106**, 7086 (2002).
79. N. I. Hammer, E. G. Diken, J. R. Roscioli, M. A. Johnson, E. M. Myshakin, K. D. Jordan, A. B. McCoy, X. Huang, J. M. Bowman, and S. Carter, *J. Chem. Phys.* **122**, 244301 (2005).

80. J. M. Headrick, E. G. Diken, R. S. Walters, N. I. Hammer, R. A. Christie, J. Cui, E. M. Myshakin, M. A. Duncan, M. A. Johnson, and K. D. Jordan, *Science* **308**, 1765 (2005).
81. R. C. Dunbar, *Int. J. Mass Spectrom.* **200**, 571 (2000).
82. R. L. Grimm, J. B. Mangrum, and R. C. Dunbar, *J. Phys. Chem. A* **108**, 10897 (2004).
83. T. J. Selegue and J. M. Lisy, *J. Phys. Chem.* **96**, 4143 (1992).
84. J. M. Lisy, *Int. Rev. Phys. Chem.* **16**, 267 (1997).
85. O. M. Cabarcos, C. J. Weinheimer, and J. M. Lisy, *J. Chem. Phys.* **108**, 5151 (1998).
86. T. D. Vaden, B. Forinash, and J. M. Lisy, *J. Chem. Phys.* **117**, 4628 (2002).
87. T. D. Vaden, C. J. Weinheimer, and J. M. Lisy, *J. Chem. Phys.* **121**, 3102 (2004).
88. T. D. Vaden, J. M. Lisy, P. D. Carnegie, E. D. Pillai, and M. A. Duncan, *Phys. Chem. Chem. Phys.* **8**, 3078 (2006).
89. E. J. Bieske and O. Dopfer, *Chem. Rev.* **100**, 3963 (2000).
90. D. A. Wild, R. L. Wislon, P. S. Weiser, and E. J. Bieske, *J. Chem. Phys.* **113**, 10154 (2000).
91. D. A. Wild, Z. M. Loh, P. P. Wolynec, P. S. Weiser, and E. J. Bieske, *Chem. Phys. Lett.* **332**, 531 (2000).
92. G. H. Wu, J. G. Guan, G. D. C. Aitken, H. Cox, and A. J. Stace, *J. Chem. Phys.* **124**, 201103 (2006).
93. P. Maitre, S. Le Caer, A. Simon, W. Jones, J. Lemaire, H. N. Mestdagh, M. Heninger, G. Mauclaire, P. Boissel, R. Prazeres, F. Glotin, and J. M. Ortega, *Nucl. Instrum. Meth. A* **507**, 541 (2003).
94. A. Simon, W. Jones, J. M. Ortega, P. Boissel, J. Lemaire, and P. Maitre, *J. Am. Chem. Soc.* **126**, 11666 (2004).
95. R. S. Walters, T. D. Jaeger, and M. A. Duncan, *J. Phys. Chem. A* **106**, 10482 (2002).
96. J. Oomens, B. G. Sartakov, G. Meijer, and G. Von Helden, *Int. J. Mass Spectrom.* **254**, 1 (2006).
97. L. R. Thorne and J. L. Beauchamp, in *Gas Phase Ion Chemistry*, M. T. Bowers (ed.), Academic Press, Orlando, FL, 1984, vol. **3**, pp. 41.
98. S. K. Shin and J. L. Beauchamp, *J. Am. Chem. Soc.* **112**, 2057 (1990).
99. P. I. Surya, L. M. Roth, D. R. A. Ranatunga, and B. S. Freiser, *J. Am. Chem. Soc.* **118**, 1118 (1996).
100. P. I. Surya, D. R. A. Ranatunga, and B. S. Freiser, *J. Am. Chem. Soc.* **119**, 3351 (1997).
101. G. Dietrich, S. Kruckeberg, K. Lutzenkirchen, L. Schweikhard, and C. Walther, *J. Chem. Phys.* **112**, 752 (2000).
102. G. Gregoire and M. A. Duncan, *J. Chem. Phys.* **117**, 2120 (2002).
103. M. Okumura, L. I. Yeh, J. D. Meyers, and Y. T. Lee, *J. Chem. Phys.* **85**, 2328 (1986).
104. P. Ayotte, G. H. Weddle, J. Kim, and M. A. Johnson, *J. Am. Chem. Soc.* **120**, 12361 (1998).
105. P. Ayotte, C. G. Bailey, J. Kim, and M. A. Johnson, *J. Chem. Phys.* **108**, 444 (1998).
106. P. Ayotte, J. Kim, J. A. Kelley, S. B. Nielsen, and M. A. Johnson, *J. Am. Chem. Soc.* **121**, 6950 (1999).
107. S. A. Corcelli, J. A. Kelley, J. C. Tully, and M. A. Johnson, *J. Phys. Chem. A* **106**, 4872 (2002).
108. R. S. Walters, N. R. Brinkmann, H. F. Schaefer, and M. A. Duncan, *J. Phys. Chem. A* **107**, 7396 (2003).
109. R. S. Walters and M. A. Duncan, *Aust. J. Chem.* **57**, 1145 (2004).
110. G. Gregoire, N. R. Brinkmann, D. van Heijnsbergen, H. F. Schaefer, and M. A. Duncan, *J. Phys. Chem. A* **107**, 218 (2003).

111. N. R. Walker, R. S. Walters, M. K. Tsai, K. D. Jordan, and M. A. Duncan, *J. Phys. Chem. A* **109**, 7057 (2005).
112. N. R. Walker, R. S. Walters, and M. A. Duncan, *J. Chem. Phys.* **120**, 10037 (2004).
113. K. R. Asmis, G. Meijer, M. Mrümmer, C. Kaposta, G. Santambrogio, L. Wöste, and J. Sauer, *J. Chem. Phys.* **120**, 6461 (2004).
114. R. C. Dunbar, in *Gas Phase Ion Chemistry*, M. T. Bowers (ed.), Academic Press, Orlando, FL, 1984, vol. **3**, pp. 129.
115. F. F. Crim, *Annu. Rev. Phys. Chem.* **44**, 397 (1993).
116. A. Bach, J. M. Hutchison, R. J. Holiday, and F. F. Crim, *J. Chem. Phys.* **116**, 4955 (2002).
117. A. Callegari and T. R. Rizzo, *Chem. Soc. Rev.* **30**, 214 (2001).
118. I. Bar and S. Rosenwaks, *Int. Rev. Phys. Chem.* **20**, 711 (2001).
119. C. Tao and P. J. Dagdigian, *Chem. Phys. Lett.* **350**, 63 (2001).
120. O. Votava, D. F. Plusquellic, and D. J. Nesbitt, *J. Chem. Phys.* **110**, 8564 (1999).
121. F. Aguirre, J. Husband, C. J. Thompson, and R. B. Metz, *Chem. Phys. Lett.* **318**, 466 (2000).
122. J. Haggin, *Chem. & Eng. News* **71**, 27 (1993).
123. R. H. Crabtree, *Chem. Rev.* **95**, 987 (1995).
124. B. K. Warren and S. T. Oyama, *Heterogeneous Hydrocarbon Oxidation*. American Chemical Society, Washington, D.C., 1996.
125. Y. Wang and K. Otsuka, *J. Chem. Soc. Chem. Commun.* **1994**, 2209 (1994).
126. Y. Wang, K. Otsuka, and K. Ebitani, *Catal. Lett.* **35**, 259 (1995).
127. H. Matsumoto, S. Tanabe, K. Okitsu, Y. Hayashi, and S. L. Suib, *J. Phys. Chem. A* **105**, 5304 (2001).
128. R. A. Periana, D. J. Taube, S. Gamble, H. Taube, T. Satoh, and H. Fujii, *Science* **280**, 560 (1998).
129. R. A. Periana, G. Bhalla, W. J. Tenn, K. J. H. Young, X. Y. Liu, O. Mironov, C. J. Jones, and V. R. Ziatdinov, *J. Mol. Catal. A* **220**, 7 (2004).
130. R. Raja and P. Ratnasamy, *Appl. Catal. A General* **158**, L7 (1997).
131. J. Haggin, *Chem. & Eng. News* **72**, 24 (1994).
132. A. C. Rosenzweig, C. A. Frederick, S. J. Lippard, and P. Nordlund, *Nature* (*London*) **366**, 537 (1993).
133. L. J. Shu, J. C. Nesheim, K. Kauffmann, E. Munck, J. D. Lipscomb, and L. Que, *Science* **275**, 515 (1997).
134. D. Schröder and H. Schwarz, *Angew. Chem. Int. Ed. Engl.* **34**, 1973 (1995).
135. H. Schwarz and D. Schröder, *Pure Appl. Chem.* **72**, 2319 (2000).
136. R. B. Metz, in *Research Advances in Physical Chemistry*, R. M. Mohan (ed.), Global, Trivandrum, 2001, vol. 2, pp. 35.
137. F. Aguirre, J. Husband, C. J. Thompson, K. L. Stringer, and R. B. Metz, *J. Chem. Phys.* **119**, 10194 (2003).
138. H. Y. Afeefy, J. F. Liebman, and S. E. Stein, in *NIST Chemistry WebBook, NIST Standard Reference Database Number 69*, W. G. Mallard and P. J. Linstrom (eds.), National Institute of Standards and Technology, Gaithersburg MD 20899, July 2001.
139. F. Aguirre, Electronic spectroscopy of Au $CH_2^+$ and intermediates involved in the conversion of methane to methanol by $FeO^+$ Ph.D. Dissertation, Dept. of Chemistry. University of Massachusetts, 2002.

140. K. Yoshizawa, Y. Shiota, and T. Yamabe, *J. Am. Chem. Soc.* **120**, 564 (1998).
141. G. Altinay, M. Citir, and R. B. Metz, to be submitted (2008).
142. K. Yoshizawa, Y. Shiota, and T. Yamabe, *Chem. Eur. J.* **3**, 1160 (1997).
143. K. Yoshizawa, Y. Shiota, and T. Yamabe, *J. Chem. Phys.* **111**, 538 (1999).
144. Y. Shiota and K. Yoshizawa, *J. Chem. Phys.* **118**, 5872 (2003).
145. Y. Shiota and K. Yoshizawa, *J. Am. Chem. Soc.* **122**, 12317 (2000).
146. A. Fiedler, D. Schröder, S. Shaik, and H. Schwarz, *J. Am. Chem. Soc.* **116**, 10734 (1994).
147. D. Schröder, A. Fiedler, M. F. Ryan, and H. Schwarz, *J. Phys. Chem.* **98**, 68 (1994).
148. M. Filatov and S. Shaik, *J. Phys. Chem. A* **102**, 3835 (1998).
149. D. Danovich and S. Shaik, *J. Am. Chem. Soc.* **119**, 1773 (1997).
150. D. Schröder, S. Shaik, and H. Schwarz, *Acc. Chem. Res.* **33**, 139 (2000).
151. D. Schröder, H. Schwarz, D. E. Clemmer, Y. Chen, P. B. Armentrout, V. Baranov, and D. K. Bohme, *Int. J. Mass Spectrom. Ion Proc.* **161**, 175 (1997).
152. A. Fiedler, J. Hrusák, W. Koch, and H. Schwarz, *Chem. Phys. Lett.* **211**, 242 (1993).
153. Y. Nakao, K. Hirao, and T. Taketsugu, *J. Chem. Phys.* **114**, 7935 (2001).
154. D. A. Chestakov, D. H. Parker, and A. V. Baklanov, *J. Chem. Phys.* **122**, 084302 (2005).
155. M. Sodupe, V. Branchadell, M. Rosi, and C. W. Bauschlicher, Jr., *J. Phys. Chem. A* **101**, 7854 (1997).
156. D. E. Lessen, R. L. Asher, and P. J. Brucat, *J. Chem. Phys.* **95**, 1414 (1991).
157. R. H. Page, Y. R. Shen, and Y. T. Lee, *J. Chem. Phys.* **88**, 4621 (1988).
158. R. N. Pribble and T. S. Zwier, *Science* **265**, 75 (1994).
159. B. Brutschy, *Chem. Rev.* **100**, 3891 (2000).
160. T. Ebata, A. Iwasaki, and N. Mikami, *J. Phys. Chem. A* **104**, 7974 (2000).
161. N. A. Macleod and J. P. Simons, *Phys. Chem. Chem. Phys.* **5**, 1123 (2003).
162. E. Nir, I. Hunig, K. Kleinermanns, and M. S. de Vries, *ChemPhysChem* **5**, 131 (2004).
163. M. Citir and R. B. Metz, *J. Chem. Phys.*, accepted to appear in vol 127 (2007).
164. K. K. Irikura and J. L. Beauchamp, *J. Phys. Chem.* **95**, 8344 (1991).
165. M. Citir and R. B. Metz, to be submitted (2008).
166. R. H. Schultz and P. B. Armentrout, *Organometallics* **11**, 828 (1992).
167. M. Hendrickx, K. Gong, and L. Vanquickenborne, *J. Chem. Phys.* **107**, 6299 (1997).
168. R. H. Schultz and P. B. Armentrout, *J. Phys. Chem.* **97**, 596 (1993).
169. Q. Zhang, P. R. Kemper, and M. T. Bowers, *Int. J. Mass Spectrom.* **210**, 265 (2001).
170. W. D. Chen, E. Poullet, J. Burie, D. Boucher, M. W. Sigrist, J. J. Zondy, L. Isaenko, A. Yelisseyev, and S. Lobanov, *Appl. Opt.* **44**, 4123 (2005).
171. D. S. Yang, *Coord. Chem. Rev.* **214**, 187 (2001).
172. V. Goncharov, L. A. Kaledin, and M. C. Heaven, *J. Chem. Phys.* **125**, 133202 (2006).
173. M. C. Heaven, *Phys. Chem. Chem. Phys.* **8**, 4497 (2006).
174. J. J. Carroll, J. C. Weisshaar, P. E. M. Siegbahn, C. A. M. Wittborn, and M. R. A. Blomberg, *J. Phys. Chem.* **99**, 14388 (1995).
175. J. J. Carroll and J. C. Weisshaar, *J. Phys. Chem.* **100**, 12355 (1996).
176. M. L. Campbell, *J. Chem. Soc. Faraday Trans.* **94**, 353 (1998).